



## Investigating the Local Atmospheric Response to a Realistic Shift in the Oyashio Sea Surface Temperature Front

DIMITRY SMIRNOV AND MATTHEW NEWMAN

*Cooperative Institute for Research in Environmental Sciences, University of Colorado, and NOAA/ESRL,  
Boulder, Colorado*

MICHAEL A. ALEXANDER

*NOAA/ESRL, Boulder, Colorado*

YOUNG-OH KWON

*Woods Hole Oceanographic Institution, Woods Hole, Massachusetts*

CLAUDE FRANKIGNOUL

*LOCEAN/IPSL, Université Pierre et Marie Curie, Paris, France*

(Manuscript received 15 April 2014, in final form 22 October 2014)

### ABSTRACT

The local atmospheric response to a realistic shift of the Oyashio Extension SST front in the western North Pacific is analyzed using a high-resolution (HR;  $0.25^\circ$ ) version of the global Community Atmosphere Model, version 5 (CAM5). A northward shift in the SST front causes an atmospheric response consisting of a weak surface wind anomaly but a strong vertical circulation extending throughout the troposphere. In the lower troposphere, most of the SST anomaly-induced diabatic heating ( $\dot{Q}$ ) is balanced by poleward transient eddy heat and moisture fluxes. Collectively, this response differs from the circulation suggested by linear dynamics, where extratropical SST forcing produces shallow anomalous heating balanced by strong equatorward cold air advection driven by an anomalous, stationary surface low to the east. This latter response, however, is obtained by repeating the same experiment except using a relatively low-resolution (LR;  $1^\circ$ ) version of CAM5. Comparison to observations suggests that the HR response is closer to nature than the LR response. Strikingly, HR and LR experiments have almost identical vertical profiles of  $\dot{Q}$ . However, diagnosis of the diabatic quasigeostrophic vertical pressure velocity ( $\omega$ ) budget reveals that HR has a substantially stronger  $\nabla^2\dot{Q}$  response, which together with upper-level mean differential thermal advection balances stronger vertical motion. The results herein suggest that changes in transient eddy heat and moisture fluxes are critical to the overall local atmospheric response to Oyashio Front anomalies, which may consequently yield a stronger downstream response. These changes may require the high resolution to be fully reproduced, warranting further experiments of this type with other high-resolution atmosphere-only and fully coupled GCMs.

### 1. Introduction

Large-scale extratropical ocean–atmosphere interaction has long been recognized as dominated by atmospheric forcing of the ocean (Davis 1976; Frankignoul and Hasselmann 1977; Frankignoul 1985). However,

ocean–atmosphere coupling varies considerably across the midlatitude ocean basins, with oceanic processes likely to be more important to sea surface temperature (SST) variability in the vicinity of the western boundary currents (WBCs) and their associated SST fronts (Qiu 2000; Nonaka and Xie 2003; Small et al. 2008; Minobe et al. 2010; Kwon et al. 2010). In the North Pacific, low-frequency WBC anomalies are primarily forced by previous basin-scale wind stress fluctuations via oceanic Rossby wave propagation (Frankignoul et al. 1997; Deser

---

*Corresponding author address:* Dmitry Smirnov, NOAA/ESRL, 325 Broadway, R/PSD1, Boulder, CO 80305.  
E-mail: chillwx@gmail.com

et al. 1999; Qiu 2000; Schneider and Miller 2001). Smirnov et al. (2014) estimated that 40%–60% of SST variability in the Kuroshio–Oyashio Extension (KOE) region is driven by oceanic processes, whereas outside of the KOE most SST variability is atmosphere driven. A key outstanding question is the extent to which these ocean-driven SST anomalies impact the atmosphere, beyond the basic thermodynamic air–sea coupling via turbulent boundary layer heat flux exchange that operates throughout the extratropics (Barsugli and Battisti 1998; Frankignoul et al. 1998; Lee et al. 2008). The answer to this question is key to the relevance of large-scale extratropical coupled air–sea modes and could have repercussions on predictability, especially on decadal time scales (Schneider and Miller 2001; Qiu et al. 2014).

Major storm tracks are organized along or just downstream of the main oceanic frontal zones (Nakamura et al. 2004), suggesting that SST variations near the fronts may affect storm-track activity and the westerly jets. Some recent modeling and observational evidence supports the view that extratropical SST fronts affect the climatological atmospheric state and its variability in the North Pacific (Xu et al. 2011; Sasaki et al. 2012), North Atlantic (Minobe et al. 2008; Minobe et al. 2010), Southern Ocean (Nonaka et al. 2009; Small et al. 2014), and idealized aquaplanet experiments (Brayshaw et al. 2008; Nakamura et al. 2008), although how this impact compares to other topographic effects, including land–sea contrasts, remains unclear (e.g., Saulière et al. 2012; Kaspi and Schneider 2013). Furthermore, a better depiction of an SST front improved the numerical simulation of observed cyclones in several studies (Jacobs et al. 2008; Booth et al. 2012). One approach to investigating the importance of SST fronts is to compare the mean climates of a model run with or without a SST front. However, by design, the smoothing functions of such “front–no front” experiments result in SST anomalies with very large amplitude (exceeding 4°C; cf. Fig. 2 in Small et al. 2014), spatial extent (e.g., SST anomalies that circumnavigate the earth in aquaplanet experiments), or both, which are never realized in observations.

In this paper, we are interested in how realistic changes in the Oyashio Extension front, which is stronger than the Kuroshio Extension front at the sea surface (Nonaka et al. 2006; Frankignoul et al. 2011, hereafter FSKA11; Taguchi et al. 2012), affect the atmosphere during boreal winter, when ocean–atmosphere heat exchange is most vigorous. There is growing evidence that KOE frontal shifts—or alternatively SST anomalies in the KOE region—have a significant influence on the large-scale atmospheric circulation in the Northern Hemisphere (Liu et al. 2006; Frankignoul and Sennéchaël 2007; Qiu et al. 2007; Okajima et al. 2014). Using a lag of 2–6 months,

FSKA11 found that the Oyashio Extension SST frontal shift tends to lead an atmospheric pattern resembling the North Pacific Oscillation, a meridional dipole with centers near the date line at approximately 35° and 60°N. However, the use of monthly averaged data and a short record (1982–2008) resulted in a marginal signal to noise ratio and showed some sensitivity to seasonality. An even stronger sensitivity to seasonality, both in observations and in a coupled model, was shown by Taguchi et al. (2012), who found a high over the Gulf of Alaska and northward shift in the storm track in response to positive KOE SST anomalies in January but not in February. Gan and Wu (2013) observed a weakening of the storm track when the KOE is anomalously warm during early but not late winter. O’Reilly and Czaja (2015) found that, when the Kuroshio Extension exhibits a stronger SST front, the atmospheric heat transport by transient eddies is increased in the western Pacific and decreased in the east.

Theoretical and simple modeling studies of the extratropics (Hoskins and Karoly 1981; Hendon and Hartmann 1982; Hall et al. 2001) have shown that the large-scale steady linear atmospheric response to an extratropical SST anomaly, as represented by a low-level diabatic heating anomaly, is a slightly downstream surface cyclonic anomaly. Because of time-mean meridional temperature gradients in the midlatitudes, this circulation balances the SST-induced warming with cold air advection. This results in subsidence (excluding boundary layer Ekman pumping) over the SST anomaly, as column shrinking is required to conserve vorticity and balance the equatorward flow, yielding a baroclinic structure with a downstream upper-level high. This basic picture does not tend to support a prominent large-scale atmospheric response to extratropical SST forcing, in contrast to tropical SST forcing of deep anomalous heating, which is balanced by vertical motion whose corresponding upper-level vorticity forcing yields a more pronounced downstream Rossby wave response (Hoskins and Karoly 1981; Sardeshmukh and Hoskins 1988).

The consensus view of the atmospheric response to extratropical SST anomalies (e.g., Kushnir et al. 2002) has been that nonlinear dynamics are essential for the atmospheric response to be significant: specifically, transient eddy vorticity fluxes must act both to amplify the downstream response and modify it to be equivalent barotropic (Ting 1991; Peng et al. 1997; Hall et al. 2001; Peng and Robinson 2001; Watanabe et al. 2006). Unfortunately, these studies have otherwise yielded inconsistent results, so that their interpretation is complicated by sensitivity to many other factors. For example, a pronounced dependence on seasonality is common, possibly as a consequence of the sensitivity of the downstream response to

transient eddy feedbacks (Kushnir et al. 2002). Another issue with past fixed SST experiments is that to get a meaningful response, unrealistically strong SST anomalies have often been prescribed [e.g., Peng et al. 1997; Inatsu et al. 2003; Liu and Wu 2004; see also studies discussed by Kushnir et al. (2002)]. This implies that realistic SST anomalies would have caused a weak response, although such an approach has been rationalized by suggesting that insufficient model resolution has led to the systematic underestimation of the eddy processes and their amplifying effect. Peng et al. (1997) suggested that relatively higher-resolution general circulation models (GCMs) tended to give more consistent results in showing an anomalous equivalent barotropic ridge downstream of positive SST anomalies (broadly consistent with observations). However, at that time, even higher-resolution models had  $2^\circ+$  ( $\sim 250$  km) resolution. More recently, Jung et al. (2012) showed that reducing horizontal grid size from 126 to 39 km in a global climate model produces large improvement in its seasonal forecast skill, with much smaller additional improvement when grid size is further decreased to 16 km and even 10 km. Similar results are found for climate and regional model representation of extratropical cyclone intensity (e.g., Catto et al. 2010; Willison et al. 2013). Also, higher-resolution regional models appear to better represent the impacts of SST fronts on the atmosphere (e.g., Doyle and Warner 1993; Taguchi et al. 2009; Woollings et al. 2010; Brachet et al. 2012).

This study attempts to address the following: (i) Is a state-of-the-art GCM able to produce a robust atmospheric response to a realistic shift in the Oyashio SST front? (ii) Does this response depend on the horizontal resolution of the GCM? (iii) What physical mechanism(s) governs the local atmospheric response? We investigate the first question by prescribing an SST anomaly that corresponds to an observed shift of the Oyashio Extension front, in the KOE region only, as forcing in a global atmospheric GCM; the impact of resolution is then addressed by running identical experimental ensembles with either a  $1^\circ$  ( $\sim 90$  km) or  $0.25^\circ$  ( $\sim 23$  km) grid. Our main finding is that higher atmospheric model resolution in our experiment yields a strong remote atmospheric response to anomalous surface heating from the Oyashio SST frontal shift, not so much because remote feedbacks are altered as because key aspects of the local response over the western Pacific are extremely sensitive to model resolution. Thus, in this paper we focus exclusively on diagnosis of the local response, deferring the diagnosis of the remote response to a companion paper.

The manuscript is structured as follows: In section 2, we describe the model experimental design, including how the SST forcing boundary condition is developed and prescribed in the National Center for Atmospheric

Research Community Atmosphere Model, version 5 (CAM5) GCM, and discuss how we determine observational comparisons to the model results. In section 3, the results of the Oyashio Extension frontal shift experiments using CAM5 at high ( $0.25^\circ$ ) and relatively low ( $1^\circ$ ) resolutions are presented. In section 4, we investigate the physical mechanism associated with the atmospheric response. A comparison with observations is presented in section 5. Finally, in section 6, we summarize our findings, highlight outstanding questions, and provide motivation to study the remote response.

## 2. Experimental design

### a. Specification of an appropriate Oyashio Extension frontal shift SST anomaly

The Oyashio Extension index (OEI), developed by FSKA11, is based on the leading empirical orthogonal function of the latitude of the maximum monthly averaged meridional SST gradient ( $SST_Y$ ) within the domain  $35^\circ\text{--}47^\circ\text{N}$ ,  $145^\circ\text{--}170^\circ\text{E}$ . A regression of monthly averaged SST anomalies on the OEI during the extended winter period (November–March) from 1982 to 2008 is shown in Fig. 1a. The polarity in Fig. 1a, which is associated with a northward shift in the SST front, is called the warm phase.

We are interested in the influence of this frontal shift on the large-scale atmospheric circulation, so here we force an AGCM with a prescribed SST anomaly corresponding to the frontal shift. The risk in this approach is that a substantial portion of the basinwide SST anomaly (Fig. 1a) may reflect the SST response to atmospheric changes forced by or contemporaneous with the Oyashio Extension shift, which should not be included in a prescribed SST experiment (Barsugli and Battisti 1998; Bretherton and Battisti 2000). That is, we wish to prescribe an SST anomaly that represents only oceanic forcing of the atmosphere. To focus on the direct frontal influence, we have applied the following to the anomaly in Fig. 1a: Starting with the  $140^\circ\text{E}$  meridian and progressing eastward, a 61-point ( $15.25^\circ$  span of latitude) tapered cosine window (taper ratio is 0.5) is applied in the meridional direction by centering it on the latitude where the November–March-mean  $|SST_Y|$  is maximized and only if  $|SST_Y| > 1.5^\circ\text{C}$  ( $100\text{ km}$ ) $^{-1}$  (anomalies outside of the filter are set to zero). Next, because the finescale structure in Fig. 1a may be an artifact of the short data record, a 5-point running mean filter is applied 20 times in the zonal direction only (to prevent excessive smoothing of the SST front), and then the resultant pattern is scaled by 3 to represent a  $3\sigma$  shift of the OEI index. The final SST anomaly pattern, shown in

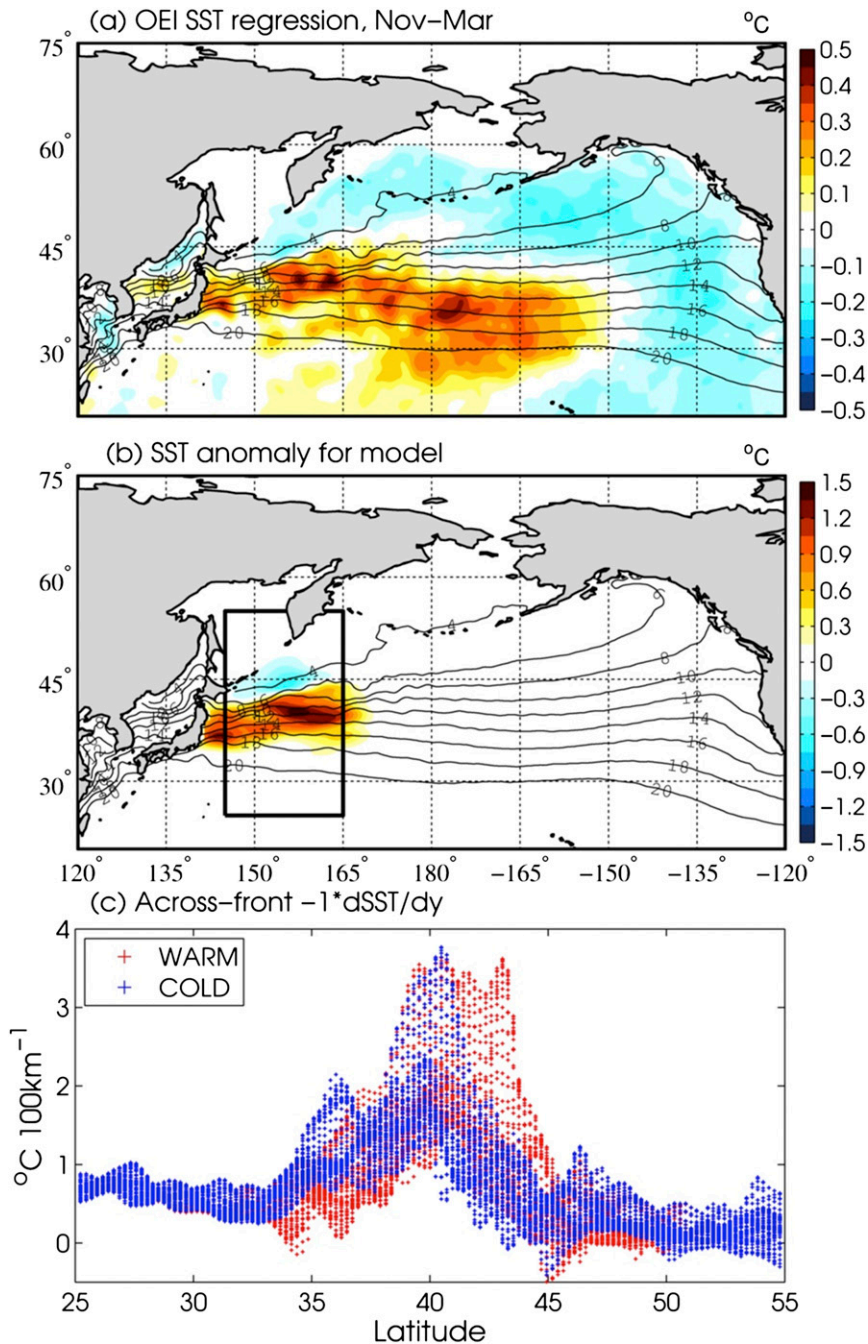


FIG. 1. (a) November–March OEI SST regression. (b) Regression after multiplying (a) by 3 and then smoothing and applying cosine-taper filter (see text). (c) Scatter of point-by-point  $-d(SST)/dy$  from 145° to 165°E as a function of latitude (dots) for the warm (red; northward Oyashio shift) and cold (blue) experiments. The black box shown in (b) shows the region used for across-front zonal averages (145°–165°E) in subsequent figures.

Fig. 1b, has SST anomalies with a maximum amplitude of  $\sim 1.5$  K but is limited to 140°–170°E. This region is where Smirnov et al. (2014) (cf. their Fig. 5a) found a significant fraction of the SST variability was forced by the ocean, presumably reflecting anomalous heat

transport via oceanic advection or eddy activity. A binned scatterplot of point-by-point  $SST_Y$  across the Oyashio Extension front over the domain marked by the box in Fig. 1b is shown in Fig. 1c. The OEI captures the northward shifted SST front [ $\sim (3^\circ\text{--}4^\circ)$  farther north in the

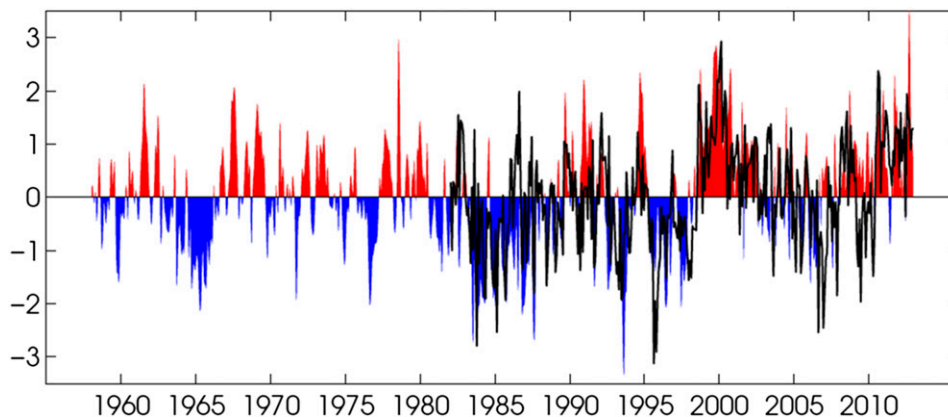


FIG. 2. Standardized POEI3 (colors) based on the  $1^{\circ}$  OAFlux SST dataset for 1958–2012 and OEI (without trend removal) from FSKA11 (black lines) for 1982–2012.

warm phase compared to the cold phase] and suggests that the front is significantly broader in meridional extent during the warm phase. However, note that the maximum SST front strength is essentially unchanged [ $\sim 3.6^{\circ}\text{C}$  ( $100\text{ km}^{-1}$ )] between the warm and cold phases.

We determine how significant these modifications of the original OEI pattern are by projecting the spatial structure shown in Fig. 1b onto observations to create a projected OEI (POEI) time series. The sensitivity of this index to different time periods and resolution is then assessed by comparing three versions constructed using 1) monthly and 2) daily averaged  $0.25^{\circ}$  resolution NOAA optimum interpolation (OI; Reynolds et al. 2007) SST anomalies from 1982 to 2012 and 3) monthly averaged  $1^{\circ}$  resolution objectively analyzed air–sea fluxes (OAFlux; Yu and Weller 2007) SST anomalies from 1958 to 2012. All resulting time series—called POEI1, POEI2, and POEI3, respectively—are standardized to unit variance. During the overlapping period (1982–2012), the two monthly averaged POEIs based on different datasets (1 and 3) have a 0.98 correlation. The correlation between the original OEI and POEI1 is only 0.56, but the indices are more strongly related (correlation of 0.77) when both are smoothed with a 13-month running mean, suggesting that while there may be nonnegligible differences between the two indices on monthly to seasonal time scales they have greater agreement on longer time scales. Moreover, the POEI3, shown in Fig. 2, has a much longer decorrelation time (7 months) compared to the OEI (3 months) so that it may represent the most persistent portion of the OEI SST anomaly and thus be more appropriate for a prescribed SST anomaly experiment. Additionally, while Fig. 1b corresponds to a  $3\sigma$  departure of the OEI, it amounts to a  $1.25\sigma$  departure of the POEI3. The correlation between the POEI1 (interpolated to daily values)

and daily POEI2 is 0.90, implying that in the daily index submonthly variability does not obscure the longer time scales. For reasons discussed in section 5, we use the daily POEI2 (hereafter just POEI) as the basis for the observational comparison to the GCM simulations.

#### b. Model details and experimental design

The CAM5 GCM (Neale et al. 2010), coupled to the Community Land Model version 2 and forced by prescribed SST and sea ice, is used for all experiments in this study. CAM5 is integrated with a finite-volume dynamical core and contains 30 unequally spaced vertical levels using a hybrid pressure–sigma coordinate system. Notably, there are approximately 8 levels within the boundary layer ( $>800$  hPa). We run two configurations of the model: a high-resolution (HR) version with  $0.25^{\circ}$  horizontal resolution and time step of 15 min and a (relatively) low-resolution (LR) version with  $1^{\circ}$  horizontal resolution and time step of 30 min. All parameterization schemes are the same between the HR and LR. Aside from the impacts of linearly interpolating the HR initial and boundary data to the LR grid (slight differences in regions of large topography), all other facets of the two models are identical.

For both configurations, a 25-member ensemble of control simulations is created in the following manner. Using 1 November initial atmospheric conditions of 25 different years taken from a previous  $0.25^{\circ}$  CAM5 simulation (Wehner et al. 2015), we run the CAM5 from 1 November through 31 March forced by the climatological, monthly averaged annual cycle of SST derived from the 1982–2011  $0.25^{\circ}$  NOAA OI dataset. The same initial land and sea ice condition are used for all ensemble members. Next, two additional sets of ensembles are conducted in very similar fashion as the control except with the addition (warm) or subtraction (cold) of

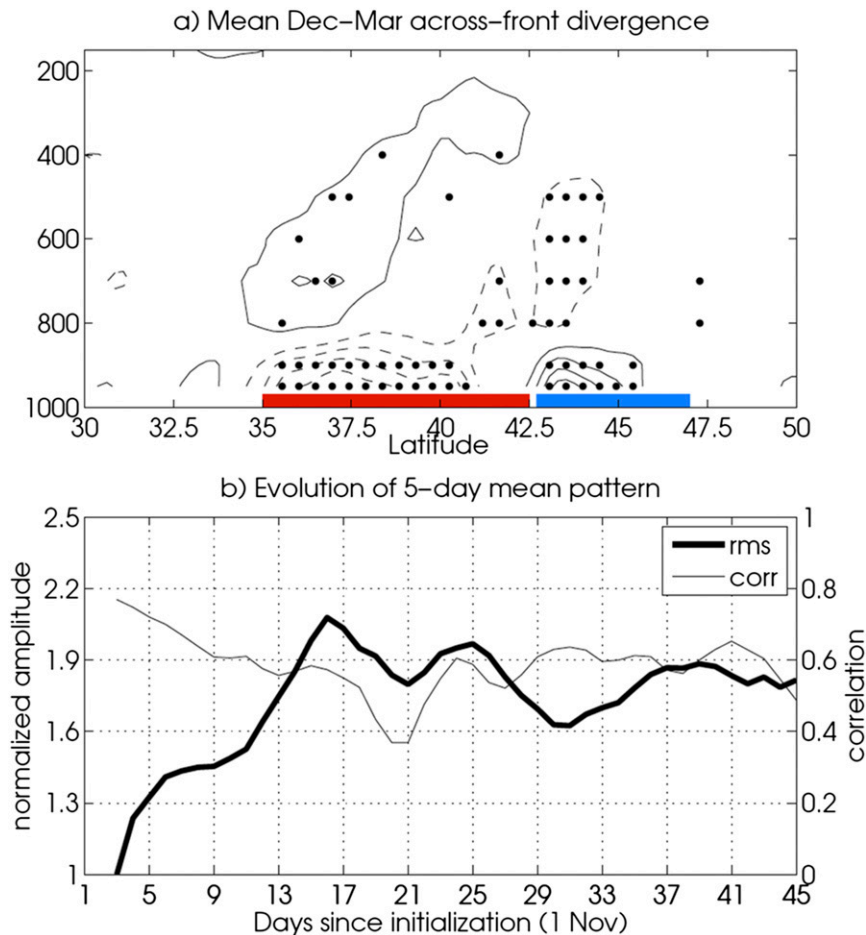


FIG. 3. (a) Mean response (contours with interval of  $4 \times 10^{-7} \text{ s}^{-1}$ ) of the December–March across-front ( $145^{\circ}$ – $165^{\circ}\text{E}$ ) divergence in the HR simulation [ordinate is pressure (hPa)]. Black dots denote areas significant at the 95% confidence level. (b) Evolution of the 5-day running mean response of across-front divergence. The thick (thin) line indicates the response pattern rms (pattern correlation) with the equilibrium pattern in (a). The rms is normalized to 1 by the day 3 value. In (a), red and blue bars denote the position of the SST anomaly.

the SST anomaly pattern shown in Fig. 1b. The SST anomaly is constant and does not evolve with the annual cycle, which can be justified by the relatively long 7-month decorrelation time scale of the monthly POEI.

### 3. Atmospheric response to an Oyashio Extension frontal shift

Since we are interested in the equilibrium winter-mean response to the Oyashio Extension shift, it is essential to determine (and discard) the time required for model spinup. Figure 3 shows that the transient atmospheric response to the northward shift of the Oyashio Extension SST front, as depicted by the spatial correlation and spatial root-mean-square to the equilibrium (December–March mean) across-front divergence, takes about 15 days to reach quasi equilibrium in the HR simulation (in LR, this takes  $\sim 20$  days; not shown). A similar

spinup time is seen when analyzing the surface (16 days) and the 2–6-day bandpass 850-hPa heat flux ( $v'T'$ ) (18 days; not shown). Importantly, in HR the response is similar from month to month and is nearly linear when comparing the warm–control and control–cold differences separately (not shown). Thus, hereafter we only discuss the mean December–March atmospheric response, determined from the mean difference between the warm and cold ensembles. Significance is assessed via the Student's  $t$  test assuming that the ensemble members are independent from each other. Finally, since the SST anomaly (warm–cold) in the model simulations represents a  $\pm 1.25\sigma$  POEI difference, the results displayed below have been rescaled to represent a  $1\sigma$  change in the POEI.

The model responses of the HR (left) and LR (right) simulations to the prescribed SST anomalies are shown in Fig. 4. The top panels show the net turbulent heat flux

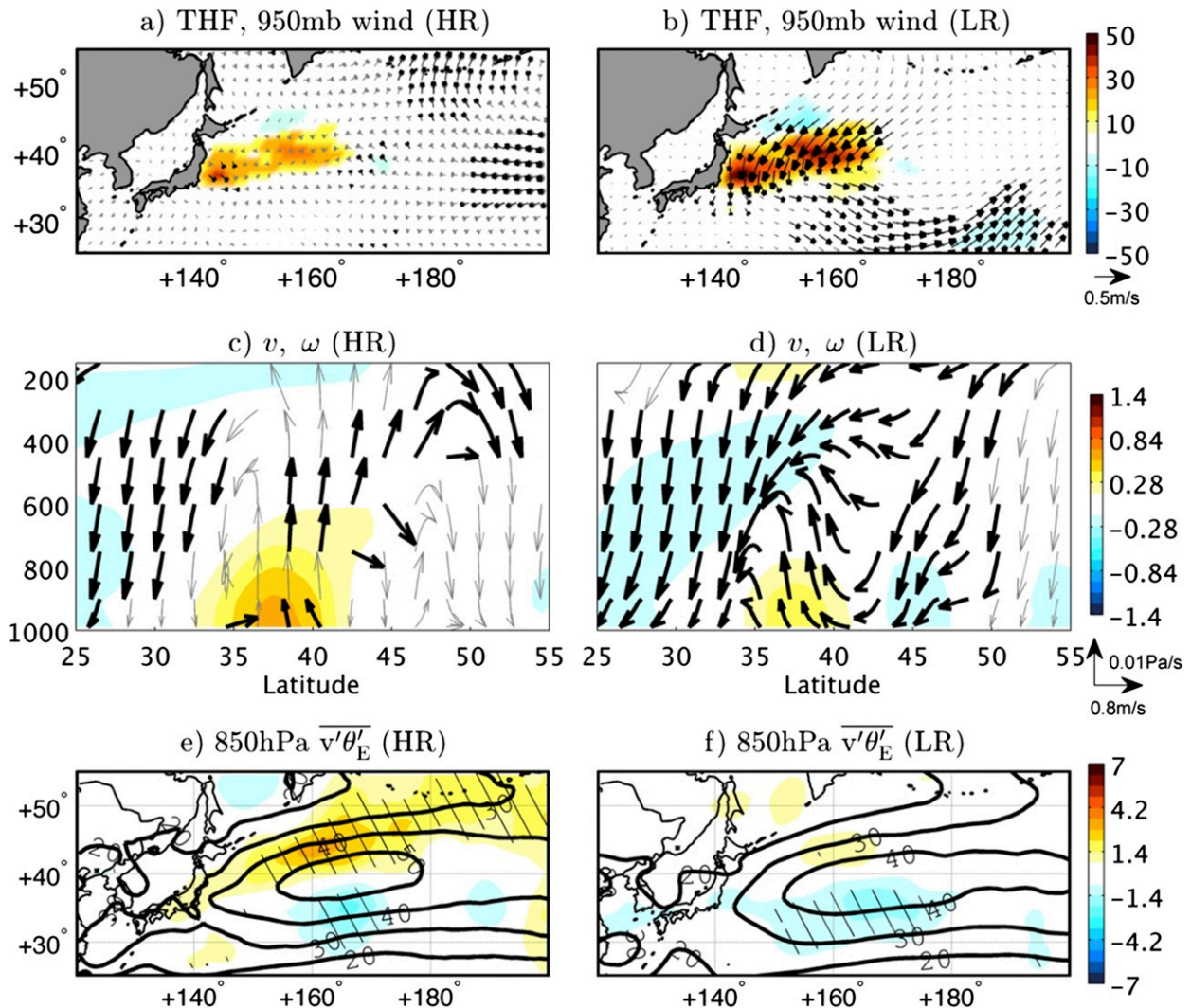


FIG. 4. The mean December–March atmospheric response (warm–cold) to a shift in the Oyashio Extension SST front in (left) HR and (right) LR simulations. (a),(b) Turbulent heat flux (colors;  $\text{K m s}^{-1}$ ) and 950-hPa wind (vectors;  $\text{m s}^{-1}$ ). Black thick vectors are significant at the 95% confidence level. (c),(d) Zonally averaged ( $145^{\circ}$ – $165^{\circ}\text{E}$ ) cross-front ( $v, \omega$ ) circulation (vectors) and  $\theta_E$  (colors) [ordinate is pressure (hPa)]. Black thick vectors are significant at the 90% confidence level. The  $\omega$  component is multiplied by 2000 to aid in visualization. (e),(f) The 850-hPa  $\overline{v'\theta'_E}$  (colors  $\text{K m s}^{-1}$ ), where stippling denotes regions significant at the 95% confidence level. The black contours indicate the mean climatological  $\overline{v'\theta'_E}$ . In all panels, the mean difference is divided by 2.5 to account for a  $\pm 1.25\sigma$  POEI SST anomaly.

(THF; positive upward) and 950-hPa wind responses for HR (Fig. 4a) and LR (Fig. 4b). Both simulations generate a surface cyclone downstream of the SST anomaly, consistent with the expected response to a shallow extratropical heat source (Hoskins and Karoly 1981; Hendon and Hartmann 1982; Peng et al. 1997; Hall et al. 2001; Deser et al. 2007; Smirnov and Vimont 2012). However, the sea level pressure (SLP) and near-surface wind responses are three to four times stronger in the LR than in the HR simulation. Furthermore, the LR surface anomalies are part of an equivalent barotropic response throughout the entire atmospheric column [not shown but similar to Pitcher

et al. (1988) and Kushnir and Lau (1992)], though it is only statistically significant from the surface through  $\sim 600$  hPa. However, there is no significant local height response in HR west of the date line. Surprisingly, the THF response in LR is 15%–20% greater than in HR. This is consistent with much stronger cold and dry air advection over the warm SST anomaly induced by the stronger LR winds compared to the HR. Consequently, while the surface heat fluxes in both the LR and HR act to damp the SST anomaly, the damping is stronger in LR. Based on the surface fluxes alone, the SST anomaly would have an  $e$ -folding time scale of 5 (4) months in the HR (LR) simulations.

While the LR shows a stronger response in the local horizontal circulation, the HR shows a substantially stronger response in the vertical circulation. Figures 4c,d show the response of the across-front zonally averaged ( $145^{\circ}$ – $165^{\circ}$ E; see box in Fig. 1b) circulation ( $v$ ,  $\omega$ ) and equivalent potential temperature  $\theta_E$ . Both HR (Fig. 4c) and LR (Fig. 4d) show upward motion over the positive SST anomalies, consistent with past studies (Feliks et al. 2004; Brachet et al. 2012), but this upward motion in HR extends to the tropopause, whereas it is limited to the lower troposphere in LR. In the upper troposphere the circulation forms two cells with northward (southward) flow north (south) of the front in HR, whereas the flow is southward at all latitudes in LR. The larger low-level  $\theta_E$  anomaly in HR over the warm SST, reflecting both warmer temperatures and enhanced low-level moisture, also reduces the low-level stability (not shown), in a region that is frequently convectively unstable (Czaja and Blunt 2011; Sheldon and Czaja 2014). The zonal wind response is weak in both simulations (not shown): in the LR, zonal wind changes are less than about  $1.5 \text{ m s}^{-1}$  and are consistent with the cyclonic circulation to the east, while the HR zonal wind changes are of opposite sign and even smaller.

In the western North Pacific, synoptic variability plays a dominant role in transporting heat and moisture (Nakamura et al. 2004; Newman et al. 2012; Kwon and Joyce 2013). Comparing the control climates of HR and LR (contours in Figs. 4e,f) with observations (see section 5) shows HR underestimates 850-hPa transient eddy meridional  $\theta_E$  flux  $\overline{v'\theta'_E}$  (which is functionally equivalent to moist static energy flux) in its core near  $40^{\circ}$ N by only about 8% ( $54 \text{ K m s}^{-1}$  in HR;  $59 \text{ K m s}^{-1}$  in ERA-Interim) while LR ( $46 \text{ K m s}^{-1}$ ) underestimates it by 22%. Unfortunately, daily humidity fields were not saved from the model output, so instead this eddy term was determined from monthly averaged covariance as  $\overline{v'\theta'_E} = \overline{v\theta_E} - \bar{v}\bar{\theta}_E$ , which includes all submonthly variability and accounts for a majority of the total climatological 850-hPa  $\overline{v'\theta'_E}$  east of Japan (not shown). Aside from the stronger mean  $\overline{v'\theta'_E}$  in the storm-track core, comparison of the HR and LR mean states does not yield any other major differences.

Both the HR and LR exhibit a northward shift of the  $\overline{v'\theta'_E}$  with a reduction south of the SST anomaly (Figs. 4e,f), but the increase north of the SST anomaly is more than 3 times stronger in the HR experiment. The total  $\overline{v'\theta'_E}$  response consists of roughly equal contributions from heat and moisture fluxes (not shown). Most of the heat flux response arises from the 2–6-day bandpass filtered, or synoptic, time scales as shown in Fig. 5 for the thermal-only component  $\overline{v'T'}$  in HR (as noted above, the bandpass moisture flux cannot be determined explicitly). In

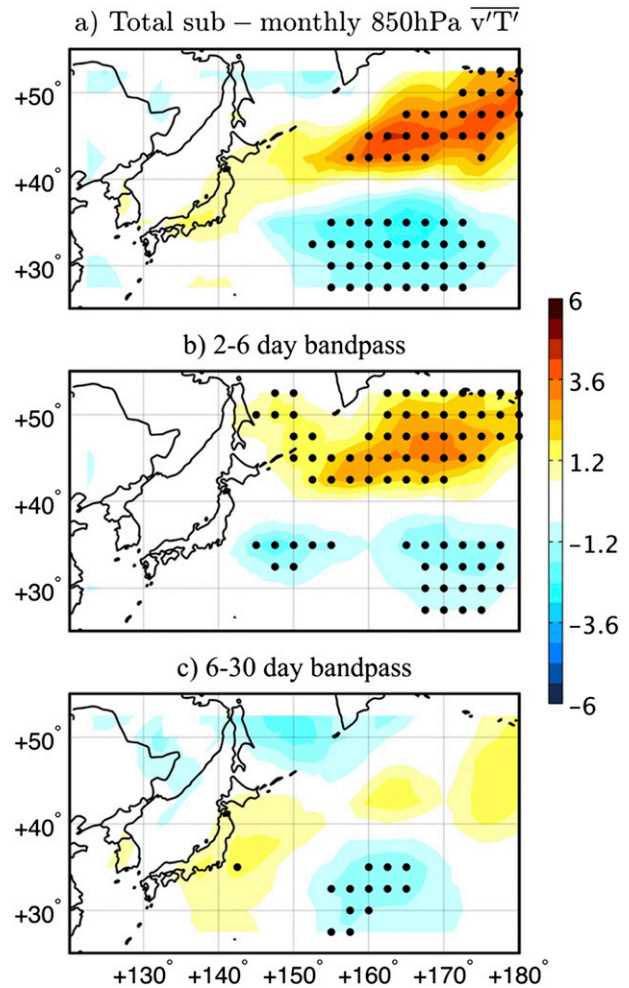


FIG. 5. (a) The total submonthly 850-hPa  $\overline{v'T'}$  ( $\text{K m s}^{-1}$ ) and its contribution separated into the (b) 2–6-day and (c) 6–30-day bandpass components in the HR simulation. Black dots denote regions that are significant at the 95% confidence level. Note that daily specific humidity output was not saved, precluding the same analysis on  $\overline{v'\theta'_E}$ .

LR the response is relatively shallow, confined mostly below about 750 hPa, whereas in the HR run the response is much deeper, extending well above 500 hPa, as shown in the across-front vertical cross sections of  $\overline{v'\theta'_E}$  (Figs. 6a,b). Equally striking differences are seen in submonthly  $\overline{v'^2}$  (Figs. 6c,d), which increases north of the front in HR but decreases south of the front in LR. The broadening of the storm track at upper levels in HR is notable and consistent with a broader SST front (Fig. 1c) but does not reach the 95% significance level. Note that the upper-level  $\overline{v'^2}$  is about 20% stronger in the HR control compared to the LR control (black contours in Figs. 6c,d), though even HR still slightly underestimates  $\overline{v'^2}$  in ERA-Interim (not shown).

Collectively, the HR simulation places a much greater emphasis on eddy transport in a region where fluxes of

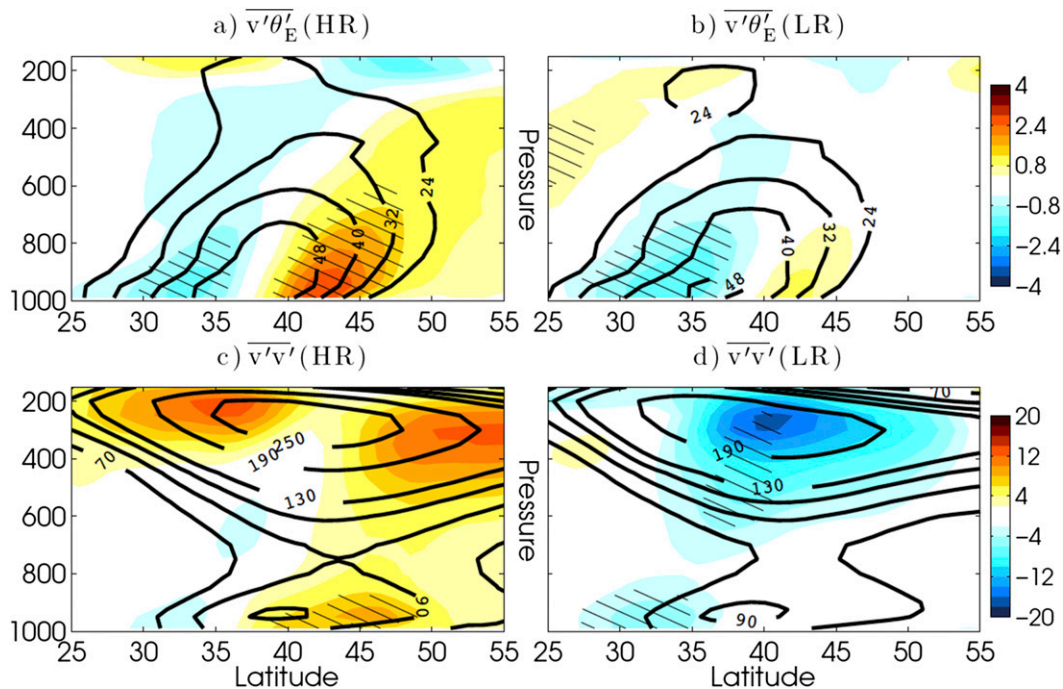


FIG. 6. Across-front mean December–March response (color shading) of (a),(b)  $\overline{v'\theta'_E}$  (shading interval is  $0.8 \text{ K m s}^{-1}$ ) and (c),(d)  $\overline{v'v'}$  (shading interval is  $2 \text{ m}^2 \text{ s}^{-2}$ ) in the (left) HR and (right) LR simulations. Stippling denotes areas that are significant at the 95% confidence level. The thick black contours show the climatological values from the (a),(c) HR and (b),(d) LR control simulations.

heat and moisture occur predominantly with the passage of warm and cold fronts (James 1995). To gauge how the HR and LR treat such passages and their sensitivity to the SST anomaly, Fig. 7 shows a composite of anomalous SLP (contour) and 2–8-day bandpass-filtered 850-hPa  $v'T'$  (color) when an atmospheric front appears in the black box shown in Figs. 7a–d (we use  $v'T'$  instead of  $v'\theta'_E$  because daily  $q$  was not archived). Fronts are identified in both the warm and cold simulations of HR and LR when the thermal front parameter (TFP), a scalar value based on the gradient of the magnitude of 6-hourly averaged 850-hPa potential temperature (see Table 1 in Hewson 1998). Using a TFP exceedance threshold value of  $0.15 \text{ K (100 km)}^{-2}$  (Renard and Clarke 1965; Booth et al. 2012), a front is identified in the box in Fig. 7 about 1 out of every 6 days. To avoid very localized, potentially misleading features, this criterion must be met at two or more neighboring grid points. Figures 7a–d show that the composite SLP field is characterized by a 6–7-hPa cyclonic anomaly within the box with a 5–6-hPa anticyclonic anomaly  $\sim 20^\circ$  east for both the warm and cold simulations of HR and LR, with  $v'T'$  consistent with northward advection of warm air in a midlatitude cyclone's warm sector. For fronts passing through this box,  $v'T'$  is about 10% stronger in the HR than LR simulations for both warm and cold phases

(cf. Figs. 7a,b; cf. Figs. 7c,d), even though the SLP composites are nearly identical, similar to the difference between the HR and LR control runs (the black contours in Figs. 4e,f). However, for the warm minus cold response (Figs. 7e,f), the SST anomaly has a much greater impact on heat flux associated with frontal passage in the HR, with a dipole in the  $v'T'$  response roughly straddling the SST front, while the LR only captures the (weaker) southern portion of the response.

Both models have enhanced cloud formation and precipitation resulting from the warm SST anomaly though the response is shifted slightly poleward (and consistent with a more robust storm-track shift) in HR compared to LR (Fig. 8). However, while the magnitude of the precipitation response is similar in HR and LR (Figs. 8a,b), the precipitable water response in HR is more than twice as large. There is also a corresponding increase in the cloud water content in the HR simulation (not shown). The much higher levels of PW and cloud water are consistent with the increased transient eddy moisture flux convergence in the HR simulation (not shown but the differences are similar to Figs. 4e,f) as well as the stronger advection of dry air from the northeast and a weakening of the background westerlies in the LR simulation (Figs. 4a,b). That is, even though the precipitation response over the SST anomaly is

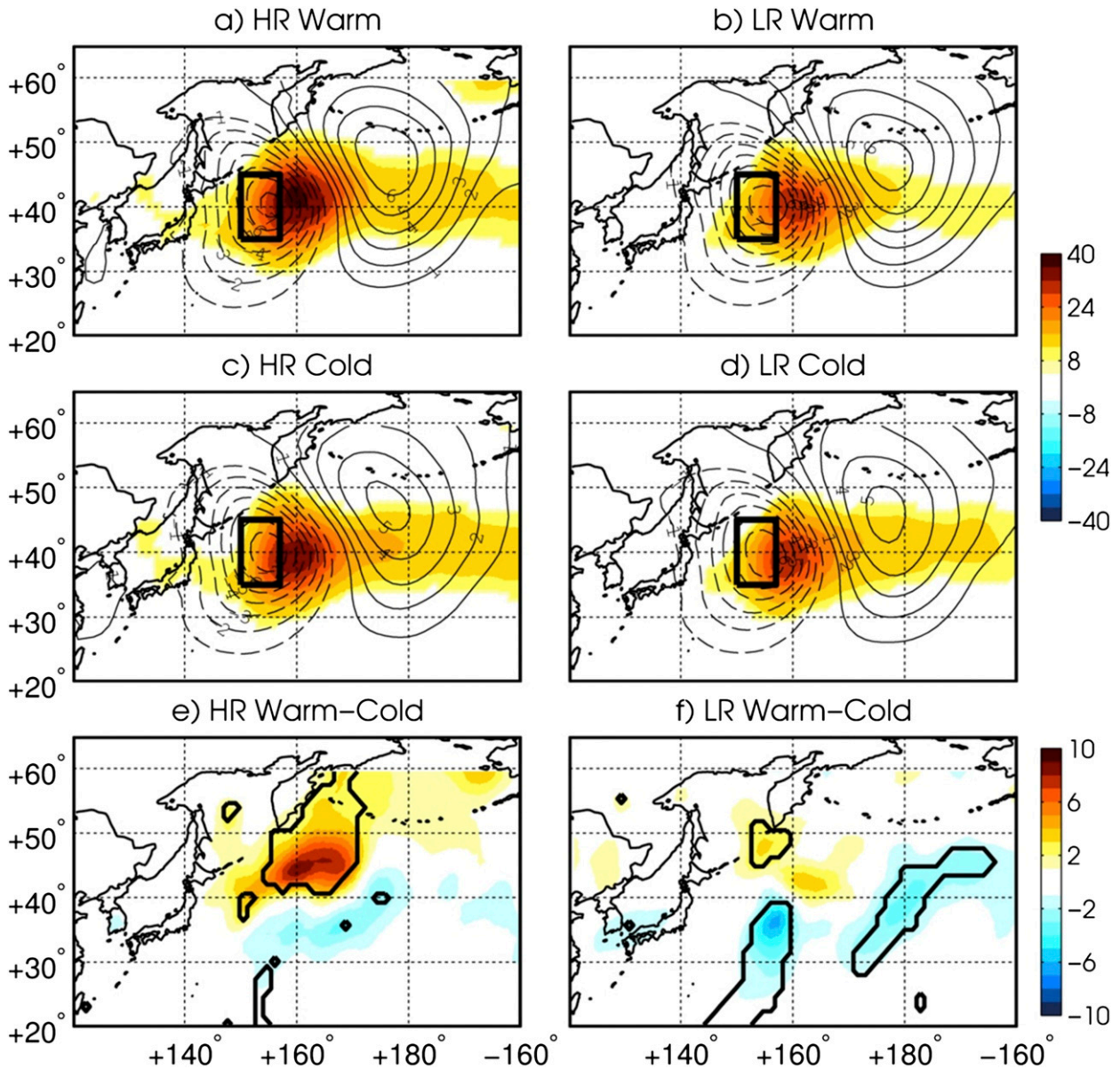


FIG. 7. (a)–(d) Composites of anomalous SLP (contours) and high-pass-filtered 850-hPa  $v'T'$  (color shading;  $\text{K m s}^{-1}$ ) on days where the thermal front parameter (see text for additional information) exceeds  $0.15 \text{ K (100 km)}^{-2}$  for the (a) warm and (c) cold HR simulations and (b) warm and (d) cold LR simulations. (e),(f) Differences of (a) – (c) and (b) – (d). In (e),(f), a thick contour encloses areas that exceed the 95% significance based on a 1000-sample Monte Carlo test. Note that SLP does not show up in (e),(f) because it does not meet the 95% significance threshold (or even the 90% threshold). Black rectangle in (a)–(d) denotes the region where the front tracking is applied (see text).

similar, in LR there is a local balance between increased evaporation and precipitation, while in HR storms converge moisture into the storm track–jet stream that can subsequently be transported downstream (not shown but see Fig. 15a,b).

Figure 9 shows the stark difference in the SLP and precipitation response from the standpoint of an individual synoptic storm. This event is chosen from the 4th day of the model runs (4 November) where a particular weather

feature could still be identified in all four simulations (warm–cold and HR–LR). One caveat is that this may not portray the sensitivity of the equilibrium response as Fig. 3 showed this requires roughly 2 weeks. Nonetheless, Fig. 9 shows that HR depicts a slightly stronger cyclone than LR, located near 40°N, 160°E. HR contains two frontal-like precipitation bands, while the LR shows one main band in the immediate vicinity of the cyclone center. However, the largest differences appear by taking

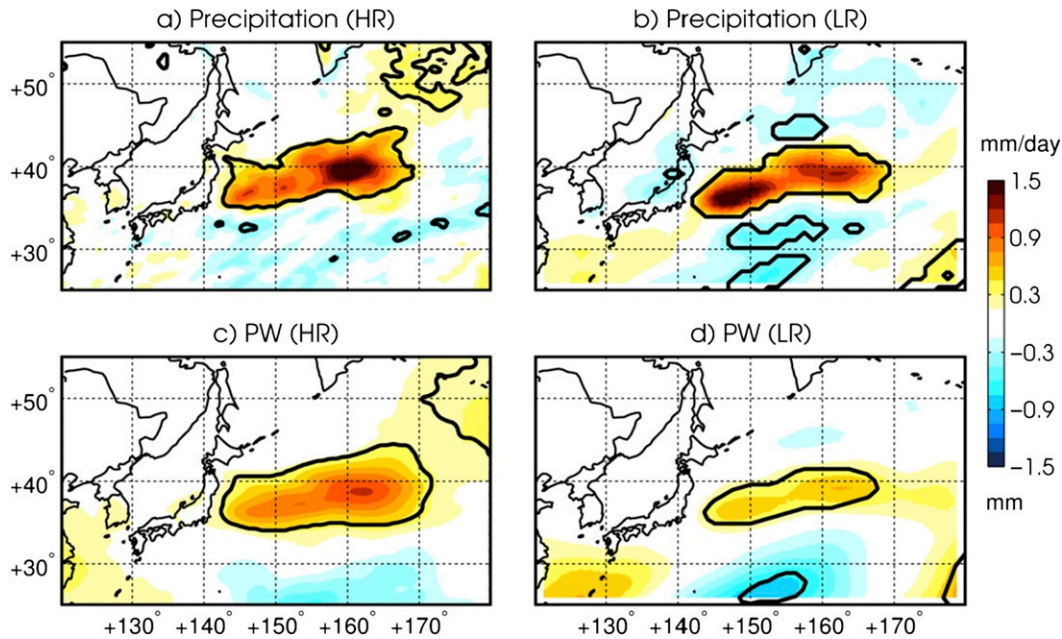


FIG. 8. Mean December–March response in (a),(b) total (convective + stratiform) precipitation ( $\text{mm day}^{-1}$ ) and (c),(d) column-integrated precipitable water (mm) in the (a),(c) HR and (b),(d) LR simulations. Contours enclose areas that are significant at the 95% confidence level.

the warm–cold response. Figures 9e,f show that the precipitation response in HR is roughly 4 times stronger and more coherent than LR, though both models depict a northward shift in precipitation to first order. Additionally, the HR shows a substantially stronger response in SLP, with a 2–3-hPa dipole straddling the cyclone center. Meanwhile, the LR shows a broader cyclonic anomaly that is located much farther west. Figure 9 is not meant to be a generalization across all synoptic disturbances, but instead shows the surprising sensitivity to atmospheric resolution at the frontal scale.

#### 4. Diagnosis of physical mechanisms

In response to the poleward shift of the SST front, the HR and LR simulations each, to different extents, develop a near-surface cyclonic circulation to the east of the warm SST anomaly, with enhanced  $\theta_E$ , upward motion, and transient eddy heat flux divergence above the SST anomaly. However, the relative importance of these processes is very different, such that, while the LR primarily balances the warm SST by a mean circulation change advecting cold and dry air southward, the HR primarily balances the enhanced heat and moisture through transient eddies transporting heat and moisture northward, probably via frontal passages. In this section, we further quantify these key differences by constructing budgets using the thermodynamic and vertical velocity ( $\omega$ ) equations.

##### a. Thermodynamic budget

First, we diagnose how heat is exchanged at the air–sea interface and within the atmospheric column. The processes that balance the diabatic heating  $\bar{Q}$  resulting from the SST anomalies are determined from the time-mean thermodynamic equation, written as

$$\begin{aligned} \underbrace{\bar{u} \frac{\partial \bar{T}}{\partial x}}_{\text{I}} + \underbrace{\frac{\partial}{\partial x} \overline{u'T'}}_{\text{II}} + \underbrace{\bar{v} \frac{\partial \bar{T}}{\partial y}}_{\text{III}} + \underbrace{\frac{\partial}{\partial y} \overline{v'T'}}_{\text{IV}} \\ + \underbrace{\left( \bar{\omega} \frac{\partial \bar{T}}{\partial p} - \frac{\kappa}{p} \bar{\omega} \bar{T} \right)}_{\text{V}} + \underbrace{\left( \overline{\omega' \frac{\partial T'}{\partial p}} - \frac{\kappa}{p} \overline{\omega' T'} \right)}_{\text{VI}} = \bar{Q}, \quad \text{VII} \end{aligned} \quad (1)$$

where overbars represent the ensemble climatological mean for each month; primes represent departures from that mean,  $\kappa = R/C_p$ , where  $R$  is  $287 \text{ J kg}^{-1} \text{ K}^{-1}$  and  $C_p$  is  $1004 \text{ J kg}^{-1} \text{ K}^{-1}$ ; and all other terms assume their typical meteorological conventions. The HR data are linearly interpolated to the LR grid and the budget is calculated for each month separately and then averaged to form a December–March mean. Term VII is from direct model output and the budget is nearly closed with the residual being a few percent of the sum from the remaining terms, except in very close proximity to orography. The warm and cold ensembles each have their own climatological means, and we calculate each term separately for the warm and cold ensembles of both HR

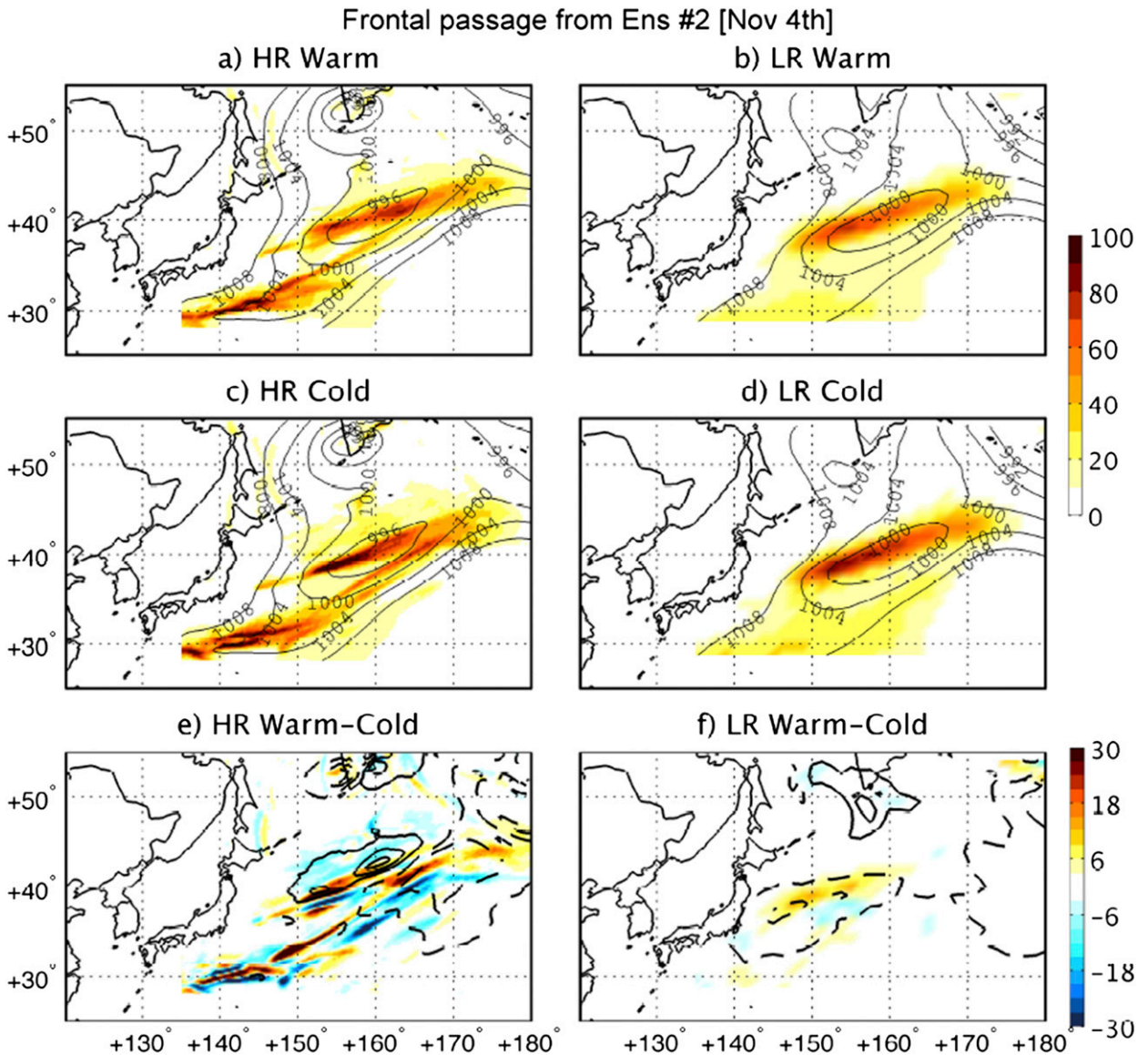


FIG. 9. Snapshot of frontal passage from 4 Nov of ensemble member 2. (a)–(d) Daily-mean SLP (contours with interval of 4 hPa) and total precipitation (color shading;  $\text{mm day}^{-1}$ ) for (top)–(bottom) the warm and cold simulations of HR and LR. (e), (f) Differences between (a) and (c) and between (b) and (d), respectively. Contour interval for SLP is 1 hPa, negative contours are dashed, and the 0 contour is omitted.

and LR. The mean difference between the warm and cold ensembles is called the response to the SST frontal shift.

Figure 10 shows the net response of the horizontal (terms I–IV), vertical (terms V and VI) and  $\bar{Q}$  components of (1) separately. In the lowest levels (1000–800 hPa),  $\omega$  is necessarily small, leaving the horizontal terms [I–IV in (1)] to balance  $\bar{Q}$ . Consistent with the stronger THF in Fig. 4b,  $\bar{Q}$  is about 15% stronger in LR than in the HR (cf. Figs. 10e,f), and therefore cooling from horizontal heat transport is also stronger. Above this layer, where  $\bar{Q}$  becomes slightly stronger in HR than LR, the most notable difference between the two simulations is that

cooling by the vertical transport terms [V–VI in (1)] is 80% stronger in HR. Indeed, vertical transport is so strong and vertically extensive in HR that above 500 hPa it must be balanced by warming from the horizontal transport terms (Fig. 10a). Little to no such net response is seen at upper levels in LR.

To differentiate between the relative importance of eddy heat flux divergence and mean thermal advection, in Fig. 11 we next show each of the seven terms in (1) averaged within the region  $35^{\circ}$ – $43^{\circ}$ N,  $145^{\circ}$ – $165^{\circ}$ E (i.e., over the positive SST anomaly; see dotted lines in Fig. 10). Near the surface the meridional heat transport

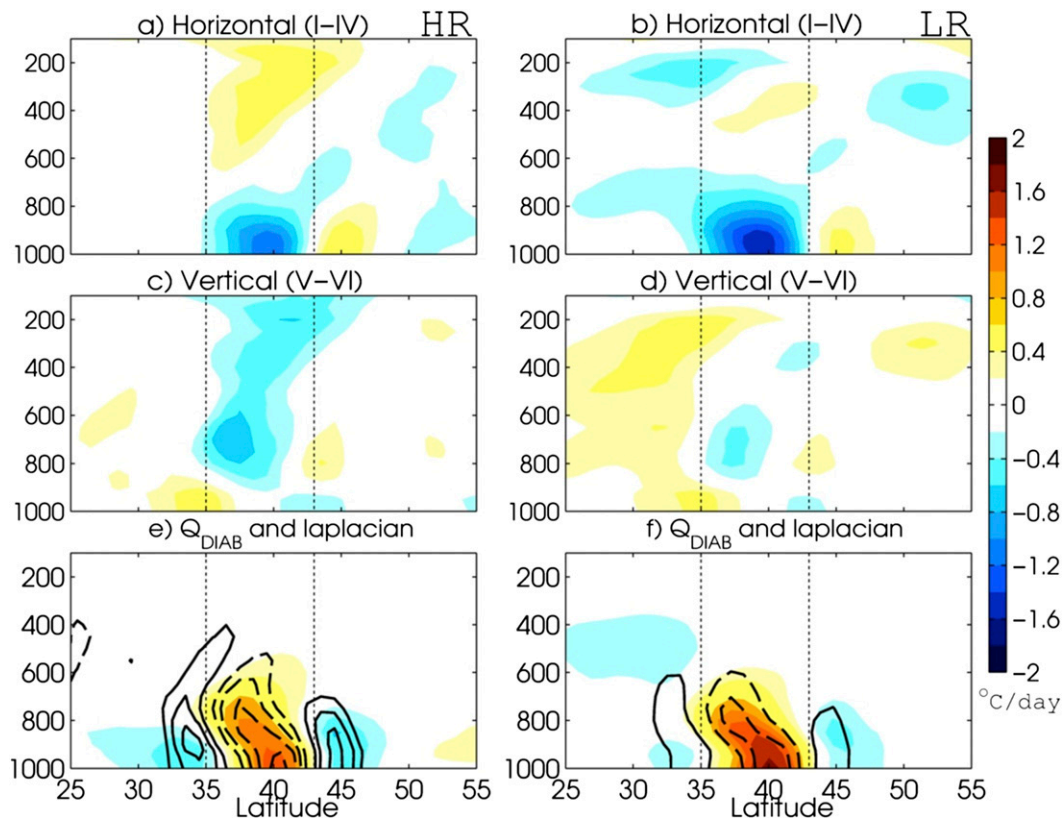


FIG. 10. Across-front December–March-mean difference of the terms comprising the thermodynamic budget in (1) for the (a),(c),(e) HR and (b),(d),(f) LR simulations [ordinate is pressure (hPa)]. (a),(b) Sum of all horizontal terms (I–IV); (c),(d) sum of all vertical terms (V and VI); and (e),(f) diabatic heating (colors) and their Laplacian (contours). The thin vertical dotted lines show the approximate latitudinal position (35°–43°N) of the positive SST anomaly and are used for meridional averaging in Fig. 11.

terms largely balance  $\bar{Q}$ , but for the LR the mean transport dominates the eddy transport whereas for the HR the eddy transport is about 60% larger than the mean transport (Fig. 11c) and has much greater vertical extent. Recall that the total (i.e., submonthly) eddy response is dominated by the 2–6-day synoptic time scales (Fig. 5). In the middle and upper troposphere, the large difference in the vertical transport between HR and LR is due to the mean  $\omega$  circulation (Fig. 11d). For the LR in this region, mean zonal and meridional terms are large but mostly offset (cf. Figs. 11b,c), whereas the primary HR balance is between the combined mean horizontal and vertical transports. Overall, the thermodynamic budget confirms that horizontal eddy transports (lower troposphere) and strong vertical motion (middle troposphere) are much more important for balancing  $\bar{Q}$  in HR than in LR simulations.

### b. Omega equation

The stronger  $\omega$  response in HR seen in Figs. 4c,d raises the question of what physical mechanism(s) correspond to this difference. To investigate, we calculate contributions

to  $\omega$  using a modified quasigeostrophic (QG) form of the generalized  $\omega$  equation that includes diabatic effects (Krishnamurti 1968; Trenberth 1978; Raisanen 1995). Unlike past studies, such as Pauley and Nieman (1992) and Raisanen (1995), we focus on the mean  $\omega$  as opposed to an individual synoptic event. The modified QG  $\omega$  equation can be written as

$$\left(\bar{\sigma}\nabla^2 + f^2\frac{\partial^2}{\partial p^2}\right)\bar{\omega} = \nabla^2 \left[ \bar{V}_g \cdot \nabla \left( -\frac{\partial\bar{\phi}}{\partial p} \right) + \overline{V'_g \cdot \nabla \left( -\frac{\partial\phi'}{\partial p} \right)} \right] + f\frac{\partial}{\partial p} \left[ \bar{V}_g \cdot \nabla (\bar{\zeta}_g + f) + \overline{V'_g \cdot \nabla \zeta'_g} \right] - \frac{\kappa}{p} \nabla^2 \bar{Q}, \quad (2)$$

where  $\sigma$  is the wintertime spatially varying December–March-mean static stability  $\sigma(x, y, p) = -(RT/p\theta)/(\partial\theta/\partial p)$  and  $\phi$  is the geopotential height. Terms I and II are the mean

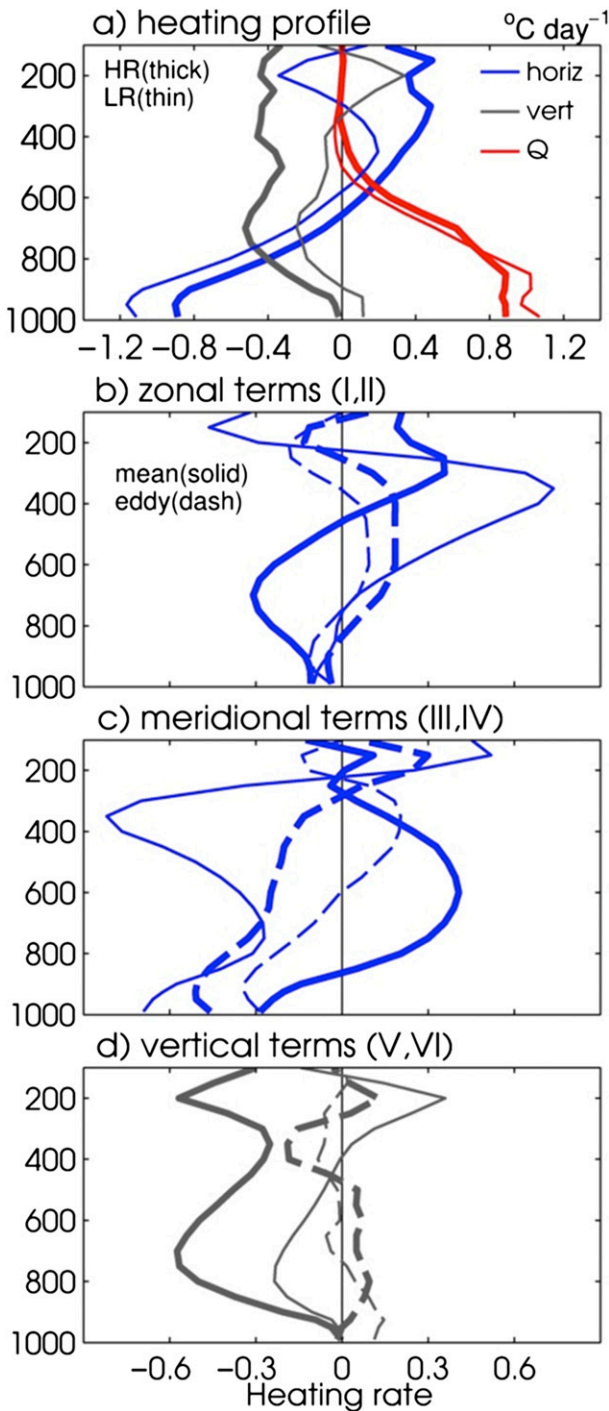


FIG. 11. Vertical profiles of the heating rate response ( $\text{K day}^{-1}$ ) arising from (a) horizontal (blue) and vertical (gray) transport, diabatic processes (red). (b)–(d) Separation from (a) of the horizontal component into mean (solid) and eddy (dash) components for zonal and meridional transport, and into mean and eddy terms, respectively. The thick (thin) lines are for HR (LR). Note the different x-axis scale in (b)–(d) compared to (a).

and eddy components of the differential thermal advection, while terms III and IV are the mean and eddy components of the differential vorticity advection. Generally, thermal (vorticity) advection is more important in the lower (mid and upper) troposphere; however, there is often strong cancellation between the two (Hoskins et al. 1978; Billingsley 1998) and investigating each term separately may be beneficial.

The recalculated  $\omega$  response ( $\omega^R$ ) is accomplished via successive relaxation by forcing with the sum of the rhs of (2). Details of the calculation are in the appendix. Figures 12a,b show the across-front response in  $\omega$  compared with  $\omega^R$  for HR and LR. There are regions where  $\omega^R$  differs from  $\omega$ , but generally this difference is less than 20%. Over the warm SST ( $36^{\circ}$ – $42^{\circ}\text{N}$ ),  $\omega^R$  overestimates the upward motion, but except near the tropopause this discrepancy is relatively small. Given this, the  $\omega^R$  response can be used as a proxy for  $\omega$  and Figs. 12c–f show the dominant terms in (2); terms II (eddy thermal), III (mean vorticity), and IV (eddy vorticity) are small (less than one contour) and thus not shown. Over the SST anomaly in the lower to middle troposphere (from the surface to 500 hPa), the HR simulation generates vertical motion that is about 40% stronger than LR and is balanced by a stronger diabatic term V. This might appear to contradict the earlier observation that the low-level LR heating is actually stronger than HR (cf. Figs. 10e,f), but it is the finer-scale structure of  $\bar{Q}$  as measured by  $\nabla^2 \bar{Q}$  (see dashed contours of Figs. 10e,f) that is commensurately stronger in HR at lower levels. That is, the narrowness of the diabatic heating balances the stronger  $\omega$  field, though causality cannot be determined via the diagnostic equation (2).

The other major difference between  $\omega^R$  in the two simulations is mainly in the middle and upper troposphere, where mean differential thermal advection [term I in (2); Figs. 12c,d] generates stronger upward motion in the HR simulation. Since this region has a significant mean meridional temperature gradient and weak poleward flow (not shown), enhanced upward motion could be maintained by a shift in the temperature gradient and/or by changes in the circulation. To determine which is more important, we recalculate  $\omega^R$  but using several modified forms of term I, as shown in Fig. 13. First, Fig. 13b shows that, when  $u$  and  $v$  are both set to be their control climatological values, the  $\omega^R$  response is much weaker and nearly of opposite sign as the full term I forcing (cf. Fig. 13a), implying that changes in the mean  $T$  field are an insignificant contributor to term I. Next, when  $T$  is set to climatology (Fig. 13c), the  $\omega^R$  is nearly identical to full forcing, confirming that the anomalous wind is responsible for balancing the upper-level  $\omega^R$ . Finally, when  $T$  and  $u$  are set to climatology (Fig. 13d),

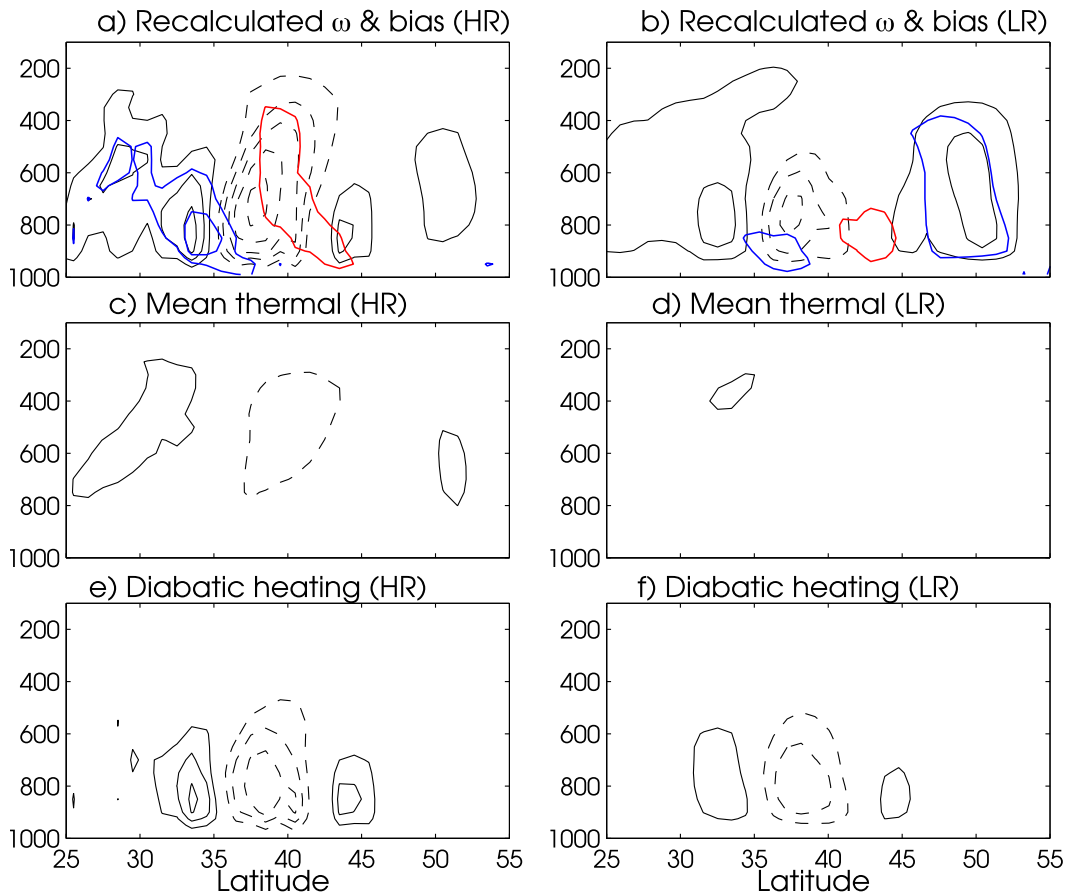


FIG. 12. (left) HR and (right) LR simulations. (a),(b) Across-front mean  $\omega^R$  (contours) and  $\omega - \omega^R$  (contours—red: positive; blue: negative), respectively. Contour interval is  $0.005 \text{ Pa s}^{-1}$ . The contribution to  $\omega^R$  decomposed into the (c),(d) mean thermal and (e),(f) diabatic heating components. The eddy thermal, mean vorticity, and eddy vorticity components are negligible ( $<1$  contour) and are not shown. See (2) for terms.

the resulting  $\omega^R$  is almost identical to the full forcing, showing that it is specifically the anomalous  $v$  that contributes most strongly to balancing the upper-level  $\omega^R$  in HR. The impact of anomalous  $u$  is not negligible and has about 20% of the impact of  $v$  but is shifted farther south than the main region of upward motion seen in Fig. 13a.

## 5. Observational comparison

Properly diagnosing extratropical air–sea interactions in observations is challenging. Simultaneous atmosphere–ocean statistics can be misleading because of the coupled nature of the problem and the differing oceanic and atmospheric dynamical time scales (Frankignoul and Hasselmann 1977). To address this issue, empirical analysis in the extratropics must include some temporal lag that is longer than the intrinsic atmospheric persistence of a few days to weeks (Frankignoul and Kestenare 2002) or, ideally, empirically estimate coupled air–sea dynamics explicitly (Smirnov et al. 2014). This is difficult

in short datasets of a multivariate system in which slowly evolving oceanic forcing may produce atmospheric responses coexisting with faster coupled air–sea variability, as well as oceanic variability forced primarily by the atmosphere, with corresponding spatial patterns that are neither identical nor orthogonal.

As noted in the introduction, past observational analyses on the impact of the Oyashio SST front find pronounced signals but do not uniformly agree, especially concerning the remote atmospheric response. We do not aim to solve that problem in this paper. However, given the strong sensitivity of the results to model resolution, it is natural to ask whether the local atmospheric response of either experiment is consistent with nature. We do not expect an identical match of course, since although the SST anomaly used in our experiment has realistic amplitude and pattern it was held fixed and specified only within the POEI region. Still, to create an observational comparison to section 3, we have regressed various atmospheric variables on the POEI for

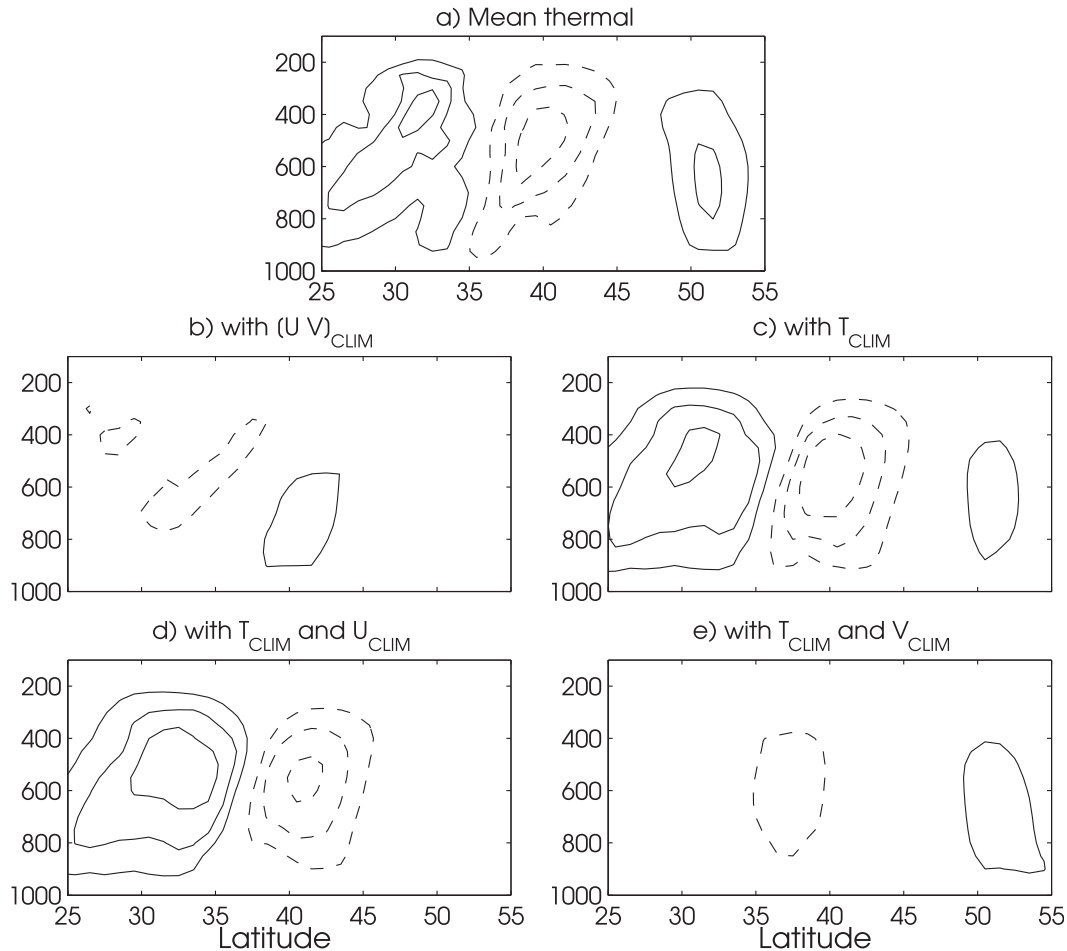


FIG. 13. (a) Mean thermal contribution to across-front  $\omega^R$  response in the HR simulation (as in Fig. 12c but with contour interval of  $0.0025 \text{ Pa s}^{-1}$ ). (b)–(e) As in (a), but setting to climatological values from the HR control simulations:  $(u, v)$ ,  $T$ ,  $(T, u)$ , and  $(T, v)$ , respectively.

lags ranging from several days to 2 months, with the POEI both leading and lagging the atmosphere, roughly similar to the FSKA11 approach. We have also examined both daily and monthly averaged data. Choosing one representative lag and data sampling interval is difficult as no single lag time captures the response of all variables, possibly because (i) there is a transient atmospheric response to the Oyashio Extension shift that is dependent on lag and (ii) each atmospheric variable decorrelates on a different time scale. For display purposes, we show a lag regression of daily wintertime (November–March) data when the POEI leads the atmosphere by 14 days, which should be long enough to mainly capture the atmospheric response to the POEI (as most atmospheric variables are nearly fully decorrelated after two weeks) and also seems appropriate based on the earlier discussion of the model response equilibration time (Fig. 3). For comparison, we also show the simultaneous regression between the atmosphere and

the POEI but note that this is difficult to interpret since it can contain both the forcing of and response to the POEI SST anomaly.

In general, the regression amplitude depends on lag, sometimes strongly, but the spatial structure is fairly consistent. Using daily data resulted in a 20%–40% stronger signal compared to using monthly data, but results are otherwise qualitatively similar (not shown). ERA-Interim does not have daily values of sensible and latent heat flux, so the  $1^\circ$  OAFlux (Yu and Weller 2007) dataset is used for these variables. Also, since El Niño–Southern Oscillation (ENSO) variability has a strong teleconnection to the North Pacific (e.g., Alexander et al. 2002), we remove the covariability with ENSO from both the POEI and all atmospheric variables by a linear regression using the daily Niño-3.4 index. This generally reduces the amplitude of regression coefficients by up to 15% (mostly east of the date line) but leaves the spatial structures unchanged.

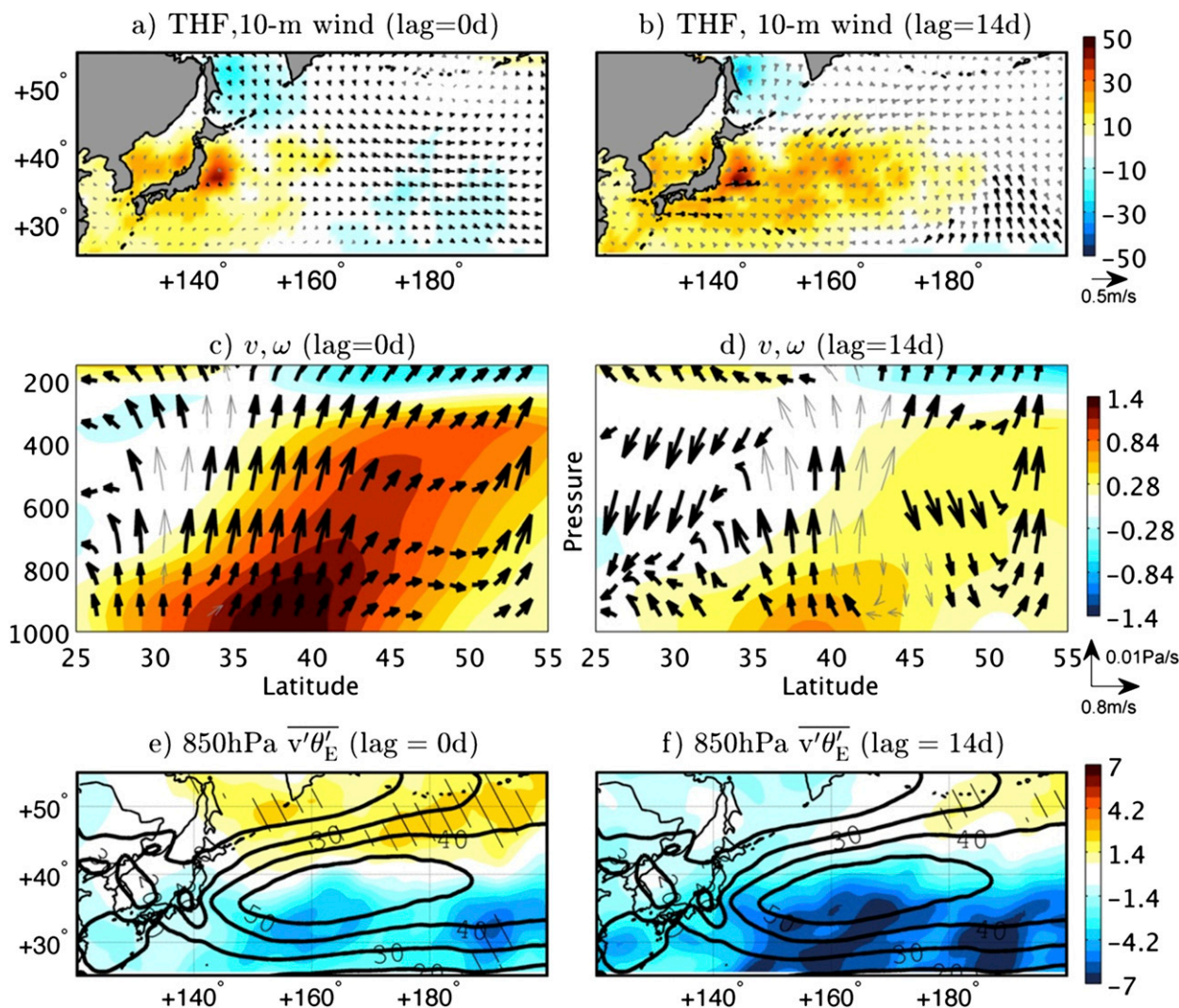


FIG. 14. Observational counterpart to Fig. 4 based on (left) simultaneous and (right) 14-day lagged regressions of the ERA-Interim atmospheric variables on the daily POEI.

Additionally, FSKA11 suggested that the meridionally confined nature of the Oyashio Extension SST front variability could make it difficult to diagnose the atmospheric response in coarse-resolution datasets. We compared the across-front regression of pressure velocity ( $\omega$ ; negative upward) on the POEI using the  $0.7^\circ$  resolution ERA-Interim (Uppala et al. 2008; [http://data-portal.ecmwf.int/data/d/interim\\_daily/](http://data-portal.ecmwf.int/data/d/interim_daily/)) dataset with the  $2.5^\circ$  resolution National Centers for Environmental Prediction Reanalysis 1 (NCEP-1; Kalnay et al. 1996) over the 1982–2012 period and found a 40% stronger signal in the former (not shown). Here we chose the enhanced ERA-Interim resolution (time range: 1979–present) over the longer data record provided by NCEP-1 (time range: 1948–present).

With the many above caveats in mind, in Fig. 14 we show the same fields as displayed in Fig. 4 but based on

regressions of observed data onto the daily POEI at 0-day (left) and 14-day lags (right). In the observed regression, positive POEI values are associated with strong THF from the ocean to atmosphere on the southern periphery of the SST front ( $36^\circ$ – $42^\circ$ N) roughly at a rate of  $\sim 30 \text{ W m}^{-2} \text{ }^\circ\text{C}^{-1}$ , consistent with previous estimates (Frankignoul and Kestenare 2002; Park et al. 2005). Note that weaker values in Fig. 14a appear to be the result of the contemporaneous state of the POEI and atmosphere, with larger values resulting when the POEI leads THF by 14 days (Fig. 14b), consistent with oceanic forcing of the atmosphere (see Fig. 21 in Frankignoul 1985). The 14-day regression (i) has a 40% weaker  $\theta_E$  signal and (ii) limits the upward vertical motion to the immediate SST anomaly region.

In general, the observations seem more broadly consistent with the HR than the LR model results. In terms of the response to POEI SST anomalies, the observed regression appears to have a broader area of upward THF than either the HR or LR simulation, which could be due to the limited spatial extent of the prescribed SST anomaly in the model, but the observed and model amplitudes appear comparable. The lack of significant wind anomalies in the observed regression appears more consistent with the HR, suggesting that LR may be overemphasizing the importance of the mean circulation response in balancing anomalous heat from the SST. Additionally, the vertical extent of the upward motion over the SST anomaly in the HR resembles the observed pattern, as does the upper-level outflow that is symmetric or slightly northward, whereas the LR (Fig. 4d) has southward flow at all levels.

Finally, both the simultaneous and 14-day lag regression (Figs. 14e,f; note that using lags of 21 and 28 days results in a very similar pattern as the 14-day lag) indicate a northward shift of  $\overline{v'\theta'_E}$  but primarily indicate a much stronger reduction of  $\overline{v'\theta'_E}$  south of the SST front, especially in Fig. 14f, which appears markedly different from Fig. 14e and appears to better match LR. However, we note that the divergence of  $\overline{v'\theta'_E}$  centered over the warm SST anomaly is the same in both panels, with the location and amplitude better matching the HR results (not shown). Collectively, it appears the observed regressions better match HR because of (i) significantly more active eddy heat transport response and (ii) deeper response in  $\omega$ .

## 6. Discussion and conclusions

In a high-resolution ( $0.25^\circ$ ) version of the NCAR CAM5, a meridional shift of the Oyashio Extension SST front is shown to locally force a robust atmospheric response dominated by changes in the eddy heat and moisture transports. However, in the corresponding low-resolution ( $1^\circ$ ) simulations, the local atmospheric response exhibits strong heating by surface fluxes that is balanced by the mean equatorward advection of cold air, consistent with the paradigm of a steady linear response to a near-surface heat source (see Hoskins and Karoly 1981). In the higher-resolution simulation, we noted a substantially weaker surface circulation (Figs. 4a,b), stronger and deeper vertical motion (Figs. 4c,d), and significantly stronger transient eddy moist static energy flux as key responses to the SST anomaly. Furthermore, it appeared that the latter difference could be seen on average in individual synoptic fronts (Figs. 7 and 9).

A number of previous modeling studies have suggested that heat from an extratropical SST anomaly is transferred into the lower troposphere where it directly

forces the atmospheric response, with transient eddy flux feedbacks primarily important for modifying the downstream upper-level circulation anomaly (Peng et al. 2003; Peng and Whitaker 1999; Hall et al. 2001; Yulaeva et al. 2001; Kushnir et al. 2002). In contrast, we find that transient eddies impact the local heat balance through changes in the transient eddy moist static energy flux. That is, extratropical cyclones respond to the underlying SST anomaly in the Oyashio Extension front region by transporting much of the anomalous heat northward, so that even under linear theory the weaker residual heating could be expected to produce only a weak surface low to the east. As the downstream low and its southward advection of cold, dry air are reduced, subsidence associated with vortex shrinking over the heating region is also reduced.

Some issues in our experimental design limit interpretation of our results. First, when comparing HR to LR responses, the impact of better resolving the SST gradient cannot be distinguished from intrinsic differences between the  $0.25^\circ$  and  $1^\circ$  versions of CAM5. This issue could be addressed by rerunning the HR experiments but with the  $1^\circ$  SST grid used by LR. Second, because some of the SST anomaly in the central and eastern Pacific related to an Oyashio Extension shift (Fig. 1a) represents coupling to or forcing by the atmosphere (Smirnov et al. 2014), we employed a conservative experimental approach by prescribing a very spatially confined SST anomaly; however, this approach still ignores potential feedbacks due to air–sea coupling. Also, the model SST anomaly is held fixed in time, whereas in observations its decorrelation time scale is 7 months and in the HR it would have a  $\sim 5$ -month decorrelation time scale if allowed to decay because of surface heat fluxes.

While it seems intuitive that the HR better resolves frontal circulations and associated  $\omega$ , we have not determined why the transient eddy heat and moisture flux responses are so sensitive to model resolution. Moist diabatic processes appear to affect how SST fronts could influence extratropical cyclone development (Fig. 9; see also Booth et al. 2012; Deremble et al. 2012; Willison et al. 2013), and Willison et al. (2013) found increased moist diabatic creation of potential vorticity during cyclogenesis between two regional model resolutions roughly corresponding to our LR and HR models. Our SST anomaly might be special in shape and/or location, such that different SST anomalies in the HR model would produce less dramatic results, although it seems reasonable to suggest that locating the SST anomaly within the climatological storm track yields a greater impact on the transient eddy heat flux than elsewhere. Moreover, our HR result could be unique to CAM5, so it should be confirmed with other high-resolution

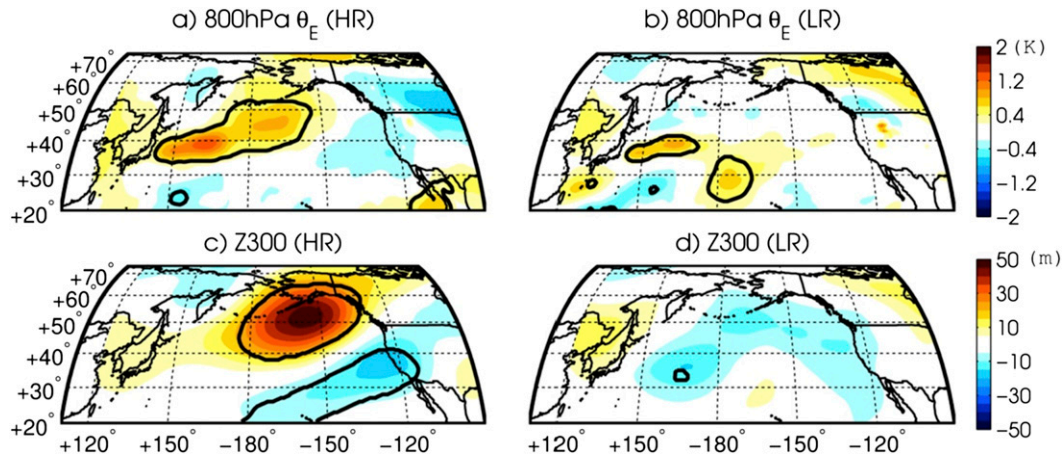


FIG. 15. Mean December–March difference in (a),(b) 800-hPa  $\theta_E$  and (c),(d) 300-hPa geopotential height over the North Pacific for the (a),(c) HR and (b),(d) LR simulations. The black contour denotes areas significant at the 95% confidence level based on a Student's  $t$  test.

GCMs. On the other hand, two recent GCM studies have shown SST frontal anomalies to have similarly pronounced impacts on transient eddy heat flux, as well as relatively weaker impacts on meridional eddy wind variance, in the North Pacific (Taguchi et al. 2009) and in the North Atlantic (Small et al. 2014). Still, our HR results (especially Figs. 7 and 9) strongly suggest that better understanding of how SST anomalies affect North Pacific cyclogenesis, including associated heat and moisture transports and how model resolution impacts the accurate simulation of these processes, is essential to determining the impact of Oyashio Extension frontal shifts in nature.

Though the focus of this paper is on the local response to the Oyashio Extension shift, it is arguably the remote response that is more relevant to society since variability in the Oyashio Extension frontal region projects onto the larger-scale Pacific decadal oscillation (Mantua et al. 1997; Schneider and Cornuelle 2005; Kwon et al. 2010; Newman 2013; Seo et al. 2014). Given the stronger and deeper local atmospheric response in the HR simulation, with a pronounced divergence anomaly located in the jet core at around 300 hPa, it is not entirely surprising that striking differences between HR and LR also exist across the entire North Pacific basin, which is shown in Fig. 15 for 800-hPa  $\theta_E$  and 300-hPa geopotential height. In HR, the  $\theta_E$  response is stronger locally and extends eastward across a substantial portion of the North Pacific, culminating with a strong anomalous anticyclone in the Gulf of Alaska and substantially reduced precipitation along the northwest coast of North American (not shown). Meanwhile, in LR, there is no significant response north of 40°N but a weak response in the subtropics as the anomalous local cyclonic circulation

advects relatively high  $\theta_E$  air southward and eastward. A full diagnosis of this remote response is underway.

*Acknowledgments.* The authors thank Justin Small and Shoshiro Minobe for stimulating discussions, as well as Hisashi Nakamura and two anonymous reviewers for constructive suggestions. Michael Wehner provided the 0.25° initial condition files for CAM5. We also gratefully acknowledge funding provided by NSF to DS and MN (AGS CLD 1035325) and Y-OK and CF (AGS CLD 1035423) and by DOE to Y-OK (DE-SC0007052).

## APPENDIX

### Details of the Modified QG $\omega$ Budget

Forcing terms I–IV in (2) only require  $\phi$  from which  $u_g$  and  $v_g$  and  $\zeta_g$  and their spatial and vertical derivatives are approximated via a centered finite-difference scheme. For the extended winter months (December–March) of the simulations, forcing terms I and III are found by separately averaging over the warm and cold ensembles during that period. Meanwhile, terms II and IV require anomalous values, which are found by removing the monthly ensemble mean separately for the warm and cold ensembles. Data are on 20 pressure levels that are log-linearly interpolated from the model hybrid (pressure and sigma) coordinates to pressure levels. Using daily averages reduces the mean thermal and momentum covariance by 20% compared to 4 times daily data, but the calculated  $\omega$  response is only altered by less than 10%. Thus, daily average data are used because of a substantial reduction in required computational time. Furthermore, the data are linearly interpolated to the LR  $\sim(1^\circ \times 1^\circ)$

grid. The effect of interpolation is only important in the immediate vicinity of topography and influences  $\omega^R$  less than 3% across the ocean grid points (not shown).

To generate  $\omega$  from (2), successive relaxation is used after imposing a zero boundary condition at the top and bottom levels as well as the horizontal boundaries of the domain [the domain is 15°–65°N, 110°–200°E; see Nieman (1990) for further details]. With this homogeneous boundary condition, the forcing from each term can be linearly separated. With a relaxation parameter (see Krishnamurti 1968; Nieman 1990) of 0.88, implying “underrelaxation,” 400 iterations are sufficient to determine  $\omega$ . The recalculated  $\omega$  ( $\omega^R$ ) is found for the warm and cold ensembles of HR and LR separately, and then the warm–cold difference is the response. Figures 12a,b show that  $\omega^R$  compares well with the model-generated  $\omega$ , with a residual less than 10% for LR and 20% for HR (except in the in localized regions in the upper levels; see Figs. 12a,b). The differences could arise from the neglect of friction terms, the use of daily averaged data that would underestimate the impact of the covariance terms, or from interpolation (only for HR as LR is calculated on its native grid). Interestingly, using the full wind (instead of the geostrophic wind) and including the tilting and twisting terms in the  $\omega$  equation (Pauley and Nieman 1992; Raisanen 1995) had very little impact on  $\omega^R$  (not shown), suggesting that the modified QG approximation with inclusion of diabatic heating yields a satisfactory approximation. This may not be the case on a storm-by-storm analysis.

#### REFERENCES

- Alexander, M. A., I. Bladé, M. Newman, J. R. Lanzante, N.-C. Lau, and J. D. Scott, 2002: The atmospheric bridge: The influence of ENSO teleconnections on air–sea interaction over the global oceans. *J. Climate*, **15**, 2205–2231, doi:10.1175/1520-0442(2002)015<2205:TABTIO>2.0.CO;2.
- Barsugli, J., and D. Battisti, 1998: The basic effects of atmosphere–ocean thermal coupling on midlatitude variability. *J. Atmos. Sci.*, **55**, 477–493, doi:10.1175/1520-0469(1998)055<0477:TBEAO>2.0.CO;2.
- Billingsley, D., 1998: A review of QG theory—Part III: A different approach. *Natl. Wea. Dig.*, **22**, 3–10.
- Booth, J. F., L. Thompson, J. Patoux, and K. A. Kelly, 2012: Sensitivity of midlatitude storm intensification to perturbations in the sea surface temperature near the Gulf Stream. *Mon. Wea. Rev.*, **140**, 1241–1256, doi:10.1175/MWR-D-11-00195.1.
- Brachet, S., F. Codron, Y. Feliks, M. Ghil, H. Le Treut, and E. Simonnet, 2012: Atmospheric circulations induced by a midlatitude SST front: A GCM study. *J. Climate*, **25**, 1847–1853, doi:10.1175/JCLI-D-11-00329.1.
- Brayshaw, D. J., B. Hoskins, and M. Blackburn, 2008: The storm-track response to idealized SST perturbations in an aquaplanet GCM. *J. Atmos. Sci.*, **65**, 2842–2860, doi:10.1175/2008JAS2657.1.
- Bretherton, C., and D. Battisti, 2000: Interpretation of the results from atmospheric general circulation models forced by the time history of the observed sea surface temperature distribution. *Geophys. Res. Lett.*, **27**, 767–770, doi:10.1029/1999GL010910.
- Catto, J. L., L. C. Shaffrey, and K. I. Hodges, 2010: Can climate models capture the structure of extratropical cyclones? *J. Climate*, **23**, 1621–1635, doi:10.1175/2009JCLI3318.1.
- Czaja, A., and N. Blunt, 2011: A new mechanism for ocean–atmosphere coupling in midlatitudes. *Quart. J. Roy. Meteor. Soc.*, **137**, 1095–1101, doi:10.1002/qj.814.
- Davis, R. E., 1976: Predictability of sea surface temperature and sea level pressure anomalies over the North Pacific Ocean. *J. Phys. Oceanogr.*, **6**, 249–266, doi:10.1175/1520-0485(1976)006<0249:POSSTA>2.0.CO;2.
- Deremble, B., G. Lapeyre, and M. Ghil, 2012: Atmospheric dynamics triggered by an oceanic SST front in a moist quasi-geostrophic model. *J. Atmos. Sci.*, **69**, 1617–1632, doi:10.1175/JAS-D-11-0288.1.
- Deser, C., M. A. Alexander, and M. S. Timlin, 1999: Evidence for a wind-driven intensification of the Kuroshio Current Extension from the 1970’s to the 1980’s. *J. Climate*, **12**, 1697–1706, doi:10.1175/1520-0442(1999)012<1697:EFAWDI>2.0.CO;2.
- , R. A. Tomas, and S. Peng, 2007: The transient atmospheric circulation response to North Atlantic SST and sea ice anomalies. *J. Climate*, **20**, 4751–4767, doi:10.1175/JCLI4278.1.
- Doyle, J. D., and T. T. Warner, 1993: The impact of the sea surface temperature resolution on mesoscale coastal processes during GALE IOP 2. *Mon. Wea. Rev.*, **121**, 313–334, doi:10.1175/1520-0493(1993)121<0313:TIOTSS>2.0.CO;2.
- Feliks, Y., M. Ghil, and E. Simonnet, 2004: Low-frequency variability in the midlatitude atmosphere induced by an oceanic thermal front. *J. Atmos. Sci.*, **61**, 961–981, doi:10.1175/1520-0469(2004)061<0961:LVITMA>2.0.CO;2.
- Frankignoul, C., 1985: Sea surface temperature anomalies, planetary waves, and air–sea feedback in the middle latitudes. *Rev. Geophys.*, **23**, 357–390, doi:10.1029/RG023i004p00357.
- , and K. Hasselmann, 1977: Stochastic climate models, Part II: Application to sea-surface temperature anomalies and thermocline variability. *Tellus*, **29**, 289–305, doi:10.1111/j.2153-3490.1977.tb00740.x.
- , and E. Kestenare, 2002: The surface heat flux feedback. Part I: Estimates from observations in the Atlantic and North Pacific. *Climate Dyn.*, **19**, 633–647, doi:10.1007/s00382-002-0252-x.
- , and N. Sennéchal, 2007: Observed influence of North Pacific SST anomalies on the atmospheric circulation. *J. Climate*, **20**, 592–606, doi:10.1175/JCLI4021.1.
- , P. Muller, and E. Zorita, 1997: A simple model of the decadal response of the ocean to stochastic wind forcing. *J. Phys. Oceanogr.*, **27**, 1533–1546, doi:10.1175/1520-0485(1997)027<1533:ASMOTD>2.0.CO;2.
- , A. Czaja, and B. L’Hedever, 1998: Air–sea feedback in the North Atlantic and surface boundary conditions for ocean models. *J. Climate*, **11**, 2310–2324, doi:10.1175/1520-0442(1998)011<2310:ASFITN>2.0.CO;2.
- , N. Sennéchal, Y. Kwon, and M. Alexander, 2011: Influence of the meridional shifts of the Kuroshio and the Oyashio Extensions on the atmospheric circulation. *J. Climate*, **24**, 762–777, doi:10.1175/2010JCLI3731.1.
- Gan, B., and L. Wu, 2013: Seasonal and long-term coupling between wintertime storm tracks and sea surface temperature in the North Pacific. *J. Climate*, **26**, 6123–6136, doi:10.1175/JCLI-D-12-00724.1.
- Hall, N. M. J., J. Derome, and H. Lin, 2001: The extratropical signal generated by a midlatitude SST anomaly. Part I: Sensitivity

- at equilibrium. *J. Climate*, **14**, 2035–2053, doi:10.1175/1520-0442(2001)014<2035:TESGBA>2.0.CO;2.
- Hendon, H. H., and D. L. Hartmann, 1982: Stationary waves on a sphere: Sensitivity to thermal feedback. *J. Atmos. Sci.*, **39**, 1906–1920, doi:10.1175/1520-0469(1982)039<1906:SWOASS>2.0.CO;2.
- Hewson, T. D., 1998: Objective fronts. *Meteor. Appl.*, **5**, 37–65, doi:10.1017/S1350482798000553.
- Hoskins, B. J., and D. J. Karoly, 1981: The steady linear response of a spherical atmosphere to thermal and orographic forcing. *J. Atmos. Sci.*, **38**, 1179–1196, doi:10.1175/1520-0469(1981)038<1179:TSLROA>2.0.CO;2.
- , I. Draghici, and H. C. Davies, 1978: A new look at the omega equation. *Quart. J. Roy. Meteor. Soc.*, **104**, 31–38, doi:10.1002/qj.49710443903.
- Inatsu, M., H. Mukougawa, and S.-P. Xie, 2003: Atmospheric response to zonal variations in midlatitude SST: Transient and stationary eddies and their feedback. *J. Climate*, **16**, 3314–3329, doi:10.1175/1520-0442(2003)016<3314:ARTZVI>2.0.CO;2.
- Jacobs, N. A., S. Raman, G. M. Lackmann, and P. P. Childs Jr., 2008: The influence of the Gulf Stream induced SST gradients on the US East Coast winter storm of 24–25 January 2000. *Int. J. Remote Sens.*, **29**, 6145–6174, doi:10.1080/01431160802175561.
- James, I. N., 1995: *Introduction to Circulating Atmospheres*. Cambridge University Press, 422 pp.
- Jung, T., and Coauthors, 2012: High-resolution global climate simulations with the ECMWF model in Project Athena: Experimental design, model climate and seasonal forecast skill. *J. Climate*, **25**, 3155–3172, doi:10.1175/JCLI-D-11-00265.1.
- Kalnay, E., and Coauthors, 1996: The NCEP/NCAR 40-Year Reanalysis Project. *Bull. Amer. Meteor. Soc.*, **77**, 437–471, doi:10.1175/1520-0477(1996)077<0437:TNYRP>2.0.CO;2.
- Kaspi, Y., and T. Schneider, 2013: The role of stationary eddies in shaping midlatitude storm tracks. *J. Atmos. Sci.*, **70**, 2596–2613, doi:10.1175/JAS-D-12-082.1.
- Krishnamurti, T. N., 1968: A diagnostic balance model for studies of weather systems of low and high latitudes, Rossby number less than 1. *Mon. Wea. Rev.*, **96**, 197–207, doi:10.1175/1520-0493(1968)096<0197:ADBMFS>2.0.CO;2.
- Kushnir, Y., and N.-C. Lau, 1992: The general circulation model response to a North Pacific SST anomaly: Dependence on time scale and pattern polarity. *J. Climate*, **5**, 271–283, doi:10.1175/1520-0442(1992)005<0271:TGCMRT>2.0.CO;2.
- , W. Robinson, I. Bladé, N. Hall, S. Peng, and R. Sutton, 2002: Atmospheric GCM response to extratropical SST anomalies: Synthesis and evaluation. *J. Climate*, **15**, 2233–2256, doi:10.1175/1520-0442(2002)015<2233:AGRTESS>2.0.CO;2.
- Kwon, Y.-O., and T. Joyce, 2013: Northern Hemisphere winter atmospheric transient eddy heat fluxes and the Gulf Stream and Kuroshio–Oyashio Extension variability. *J. Climate*, **26**, 9839–9859, doi:10.1175/JCLI-D-12-00647.1.
- , M. A. Alexander, N. A. Bond, C. Frankignoul, H. Nakamura, B. Qiu, and L. A. Thompson, 2010: Role of the Gulf Stream and Kuroshio–Oyashio systems in large-scale atmosphere–ocean interaction: A review. *J. Climate*, **23**, 3249–3281, doi:10.1175/2010JCLI3343.1.
- Lee, D., Z. Liu, and Y. Liu, 2008: Beyond thermal interaction between ocean and atmosphere: On the extratropical climate variability due to the wind-induced SST. *J. Climate*, **21**, 2001–2018, doi:10.1175/2007JCLI1532.1.
- Liu, Q., N. Wen, and Z. Liu, 2006: An observational study of the impact of the North Pacific SST on the atmosphere. *Geophys. Res. Lett.*, **33**, L18611, doi:10.1029/2006GL026082.
- Liu, Z., and L. Wu, 2004: Atmospheric response to North Pacific SST: The role of ocean–atmosphere coupling. *J. Climate*, **17**, 1859–1882, doi:10.1175/1520-0442(2004)017<1859:ARTNPS>2.0.CO;2.
- Mantua, N. J., S. R. Hare, Y. Zhang, J. M. Wallace, and R. C. Francis, 1997: A Pacific interdecadal climate oscillation with impacts on salmon production. *Bull. Amer. Meteor. Soc.*, **78**, 1069–1079, doi:10.1175/1520-0477(1997)078<1069:APICOW>2.0.CO;2.
- Minobe, S., A. Kuwano-Yoshida, N. Komori, S. Xie, and R. Small, 2008: Influence of the Gulf Stream on the troposphere. *Nature*, **452**, 206–209, doi:10.1038/nature06690.
- , —, M. Miyashita, H. Tokinaga, and S.-P. Xie, 2010: Atmospheric response to the Gulf Stream: Seasonal variations. *J. Climate*, **23**, 3699–3719, doi:10.1175/2010JCLI3359.1.
- Nakamura, H., T. Sampe, Y. Tanimoto, and A. Shimpo, 2004: Observed associations among storm tracks, jet streams and midlatitude oceanic fronts. *Earth’s Climate: The Ocean–Atmosphere Interaction, Geophys. Monogr.*, Vol. 147, Amer. Geophys. Union, 329–346.
- , —, A. Goto, W. Ohfuchi, and S.-P. Xie, 2008: On the importance of mid-latitude oceanic frontal zones for the mean state and dominant variability in the tropospheric circulation. *Geophys. Res. Lett.*, **35**, L15709, doi:10.1029/2008GL034010.
- Neale, R., and Coauthors, 2010: Description of the NCAR Community Atmosphere Model (CAM 5.0). NCAR Tech. Note NCAR/TN-486+, 224 pp.
- Newman, M., 2013: An empirical benchmark for decadal forecasts of global surface temperature anomalies. *J. Climate*, **26**, 5260–5269, doi:10.1175/JCLI-D-12-00590.1.
- , G. N. Kiladis, K. M. Weickmann, F. M. Ralph, and P. D. Sardeshmukh, 2012: Relative contributions of synoptic and low-frequency eddies to time-mean atmospheric moisture transport, including the role of atmospheric rivers. *J. Climate*, **25**, 7341–7361, doi:10.1175/JCLI-D-11-00665.1.
- Nieman, S. J., 1990: A diagnosis of non-quasigeostrophic vertical motion for a model-simulated rapidly intensifying marine extratropical cyclone. M.S. thesis, Department of Meteorology, University of Wisconsin–Madison, 181 pp.
- Nonaka, M., and S.-P. Xie, 2003: Covariations of SST and wind over the Kuroshio and its extension: Evidence for ocean-to-atmospheric feedback. *J. Climate*, **16**, 1404–1413, doi:10.1175/1520-0442(2003)16<1404:COSSA>2.0.CO;2.
- , H. Nakamura, Y. Tanimoto, T. Kagimoto, and H. Sasaki, 2006: Decadal variability in the Kuroshio–Oyashio Extension simulations in an eddy-resolving OGCM. *J. Climate*, **19**, 1970–1989, doi:10.1175/JCLI3793.1.
- , —, B. Taguchi, N. Komori, A. Kuwano-Yoshida, and K. Takaya, 2009: Air–sea heat exchanges characteristic of a prominent midlatitude oceanic front in the south Indian Ocean as simulated in a high-resolution coupled GCM. *J. Climate*, **22**, 6515–6535, doi:10.1175/2009JCLI2960.1.
- Okajima, S., H. Nakamura, K. Nishii, T. Miyasaka, and A. Kuwano-Yoshida, 2014: Assessing the importance of prominent warm SST anomalies over the midlatitude North Pacific in forcing large-scale atmospheric anomalies during 2011 summer and autumn. *J. Climate*, **27**, 3889–3903, doi:10.1175/JCLI-D-13-00140.1.
- O’Reilly, C. H., and A. Czaja, 2015: The response of the Pacific storm track and atmospheric circulation to Kuroshio Extension variability. *Quart. J. Roy. Meteor. Soc.*, doi:10.1002/qj.2334, in press.
- Park, S., C. Deser, and M. A. Alexander, 2005: Estimation of the surface heat flux response to sea surface temperature anomalies over the global oceans. *J. Climate*, **18**, 4582–4599, doi:10.1175/JCLI3521.1.

- Pauley, P. M., and S. J. Nieman, 1992: A comparison of quasigeostrophic and nonquasigeostrophic vertical motions for a rapidly intensifying marine extratropical cyclone. *Mon. Wea. Rev.*, **120**, 1108–1134, doi:10.1175/1520-0493(1992)120<1108:ACOQAN>2.0.CO;2.
- Peng, S., and J. S. Whitaker, 1999: Mechanisms determining the atmospheric response to midlatitude SST anomalies. *J. Climate*, **12**, 1393–1408, doi:10.1175/1520-0442(1999)012<1393:MDTART>2.0.CO;2.
- , and W. A. Robinson, 2001: Relationships between atmospheric internal variability and the responses to an extratropical SST anomaly. *J. Climate*, **14**, 2943–2959, doi:10.1175/1520-0442(2001)014<2943:RBAIVA>2.0.CO;2.
- , —, and M. P. Hoerling, 1997: The modeled atmospheric response to midlatitude SST anomalies and its dependence on background circulation states. *J. Climate*, **10**, 971–987, doi:10.1175/1520-0442(1997)010<0971:TMARTM>2.0.CO;2.
- , —, and S. Li, 2003: Mechanisms for the NAO responses to the North Atlantic SST tripole. *J. Climate*, **16**, 1987–2004, doi:10.1175/1520-0442(2003)016<1987:MFTNRT>2.0.CO;2.
- Pitcher, E. J., M. L. Blackmon, G. T. Bates, and S. Muñoz, 1988: The effect of North Pacific sea surface temperature anomalies on the January climate of a general circulation model. *J. Atmos. Sci.*, **45**, 173–188, doi:10.1175/1520-0469(1988)045<0173:TEONPS>2.0.CO;2.
- Qiu, B., 2000: Interannual variability of the Kuroshio Extension system and its impact on the wintertime SST field. *J. Phys. Oceanogr.*, **30**, 1486–1502, doi:10.1175/1520-0485(2000)030<1486:IVOTKE>2.0.CO;2.
- , N. Schneider, and S. Chen, 2007: Coupled decadal variability in the North Pacific: An observationally constrained idealized model. *J. Climate*, **20**, 3602–3620, doi:10.1175/JCLI4190.1.
- , S. Chen, N. Schneider, and B. Taguchi, 2014: A coupled decadal prediction of the dynamic state of the Kuroshio Extension system. *J. Climate*, **27**, 1751–1764, doi:10.1175/JCLI-D-13-00318.1.
- Raisanen, J., 1995: Factors affecting synoptic-scale vertical motions: A statistical study using a generalized omega equation. *Mon. Wea. Rev.*, **123**, 2447–2460, doi:10.1175/1520-0493(1995)123<2447:FASSVM>2.0.CO;2.
- Renard, R. J., and L. C. Clarke, 1965: Experiments in numerical objective frontal analysis. *Mon. Wea. Rev.*, **93**, 547–556, doi:10.1175/1520-0493(1965)093<0547:EINOFA>2.3.CO;2.
- Reynolds, R. W., T. M. Smith, C. Liu, D. B. Chelton, K. S. Casey, and M. G. Schlax, 2007: Daily high-resolution-blended analyses for sea surface temperature. *J. Climate*, **20**, 5473–5496, doi:10.1175/2007JCLI1824.1.
- Sardeshmukh, P. D., and B. J. Hoskins, 1988: The generation of global rotational flow by steady idealized tropical divergence. *J. Atmos. Sci.*, **45**, 1228–1251, doi:10.1175/1520-0469(1988)045<1228:TGOGRF>2.0.CO;2.
- Sasaki, Y. N., S. Minobe, T. Asai, and M. Inatsu, 2012: Influence of the Kuroshio in the East China Sea on the early summer (baiu) rain. *J. Climate*, **25**, 6627–6645, doi:10.1175/JCLI-D-11-00727.1.
- Saulière, J., D. J. Brayshaw, B. Hoskins, and M. Blackburn, 2012: Further investigation of the impact of idealized continents and SST distributions on the Northern Hemisphere storm tracks. *J. Atmos. Sci.*, **69**, 840–856, doi:10.1175/JAS-D-11-0113.1.
- Schneider, N., and A. J. Miller, 2001: Predicting western North Pacific ocean climate. *J. Climate*, **14**, 3997–4002, doi:10.1175/1520-0442(2001)014<3997:PWNPOC>2.0.CO;2.
- , and B. D. Cornuelle, 2005: The forcing of the Pacific decadal oscillation. *J. Climate*, **18**, 4355–4373, doi:10.1175/JCLI3527.1.
- Seo, H., Y.-O. Kwon, and J.-J. Park, 2014: On the effect of the East/Japan Sea SST variability on the North Pacific atmospheric circulation in a regional climate model. *J. Geophys. Res.*, **119**, 418–444, doi:10.1002/2013JD020523.
- Sheldon, L., and A. Czaja, 2014: Seasonal and interannual variability of an index of deep atmospheric convection over the western boundary currents. *Quart. J. Roy. Meteor. Soc.*, **140**, 22–30, doi:10.1002/qj.2103.
- Small, R. J., and Coauthors, 2008: Air–sea interaction over ocean fronts and eddies. *Dyn. Atmos. Oceans*, **45**, 274–319, doi:10.1016/j.dynatmoce.2008.01.001.
- , R. A. Tomas, and F. O. Bryan, 2014: Storm track response to ocean fronts in a global high-resolution climate model. *Climate Dyn.*, **43**, 805–828, doi:10.1007/s00382-013-1980-9.
- Smirnov, D., and D. J. Vimont, 2012: Extratropical forcing of tropical Atlantic variability during boreal summer and fall. *J. Climate*, **25**, 2056–2076, doi:10.1175/JCLI-D-11-00104.1.
- , M. Newman, and M. A. Alexander, 2014: Investigating the role of ocean–atmosphere coupling in the North Pacific Ocean. *J. Climate*, **27**, 592–606, doi:10.1175/JCLI-D-13-00123.1.
- Taguchi, B., H. Nakamura, M. Nonaka, and S.-P. Xie, 2009: Influences of the Kuroshio/Oyashio Extensions on air–sea heat exchanges and storm-track activity as revealed in regional atmospheric model simulations for the 2003/04 cold season. *J. Climate*, **22**, 6536–6560, doi:10.1175/2009JCLI2910.1.
- , —, —, N. Komori, A. Kuwano-Yoshida, K. Takaya, and A. Goto, 2012: Seasonal evolutions of atmospheric response to decadal SST anomalies in the North Pacific subarctic frontal zone: Observations and a coupled model simulation. *J. Climate*, **25**, 111–139, doi:10.1175/JCLI-D-11-00046.1.
- Ting, M., 1991: The stationary wave response to a midlatitude SST anomaly in an idealized GCM. *J. Atmos. Sci.*, **48**, 1249–1275, doi:10.1175/1520-0469(1991)048<1249:TSWRTA>2.0.CO;2.
- Trenberth, K. E., 1978: On the interpretation of the diagnostic quasi-geostrophic omega equation. *Mon. Wea. Rev.*, **106**, 131–137, doi:10.1175/1520-0493(1978)106<0131:OTIOTD>2.0.CO;2.
- Uppala, S., D. Dee, S. Kobayashi, P. Berrisford, and A. Simmons, 2008: Towards a climate data assimilation system: Status update of ERA-Interim. *ECMWF Newsletter*, No. 115, European Centre for Medium-Range Weather Forecasts, Reading, United Kingdom, 12–18.
- Watanabe, M., F. Jin, and L. Pan, 2006: Accelerated iterative method for solving steady problems of linearized atmospheric models. *J. Atmos. Sci.*, **63**, 3366–3382, doi:10.1175/JAS3807.1.
- Wehner, M. F., and Coauthors, 2015: The effect of horizontal resolution on simulation quality in the Community Atmospheric Model, CAM5.1. *J. Adv. Model. Earth Syst.*, doi:10.1002/2013MS000276, in press.
- Willison, J., W. A. Robinson, and G. M. Lackmann, 2013: The importance of resolving mesoscale latent heating in the North Atlantic storm track. *J. Atmos. Sci.*, **70**, 2234–2250, doi:10.1175/JAS-D-12-0226.1.
- Woollings, T., B. Hoskins, M. Blackburn, D. Hassell, and K. Hodges, 2010: Storm track sensitivity to sea surface temperature resolution in a regional atmosphere model. *Climate Dyn.*, **35**, 341–353, doi:10.1007/s00382-009-0554-3.
- Xu, H., M. Xu, S.-P. Xie, and Y. Wang, 2011: Deep atmospheric response to the spring Kuroshio over the East China Sea. *J. Climate*, **24**, 4959–4972, doi:10.1175/JCLI-D-10-05034.1.
- Yu, L., and R. Weller, 2007: Objectively analyzed air–sea heat fluxes for the global ice-free oceans (1981–2005). *Bull. Amer. Meteor. Soc.*, **88**, 527–539, doi:10.1175/BAMS-88-4-527.
- Yulaeva, E., N. Schneider, D. Pierce, and T. Barnett, 2001: Modeling of North Pacific climate variability forced by oceanic heat flux anomalies. *J. Climate*, **14**, 4027–4046, doi:10.1175/1520-0442(2001)014<4027:MONPCV>2.0.CO;2.